Prediction of noise from serrated trailing-edges

B. Lyu[1], M. Azarpeyvand[2] †
and S. Sinayoko[3]

[1]Department of Engineering, University of Cambridge, Cambridge CB2 1PZ, UK

[2]Department of Mechanical Engineering, University of Bristol, Bristol BS8 1TR, UK

[3]Institute of Sound and Vibration Research, University of Southampton, Sounthampton SO17 1BJ, UK

A new analytical model is developed for the prediction of noise from serrated trailing-edges. The model generalizes Amiet's trailing-edge noise theory to sawtooth trailing-edges, resulting in an inhomogeneous partial differential equation. The equation is then solved by means of a Fourier expansion technique combined with an iterative procedure. The solution is validated through comparison with finite element method for a variety of serrations at different Mach numbers. Results obtained using the new model predict noise reduction of up to 10 dB at 90° above the trailing-edge, which is more realistic than predictions based on Howe's model and also more consistent with experimental observations. A thorough analytical and numerical analysis of the physical mechanism is carried out and suggests that the noise reduction due to serration originates primarily from interference effects near the trailing-edge. A closer inspection of the proposed mathematical model has led to the development of two criteria for the effectiveness of the trailing-edge serrations, consistent but more general than those proposed by Howe. While experimental investigations often focus on noise reduction at ninety degrees above the trailing-edge, the new analytical model shows that the destructive interference scattering effects due to the serrations cause significant noise reduction at large polar angles, near the leading edge. It has also been observed that serrations can significantly change the directivity characteristics of the aerofoil at high frequencies and even lead to noise increase at high Mach numbers.

1. Introduction

The past few decades has seen a rapid growth of air traffic, while the public's attention to aircraft noise and its health consequences has also been continuously increasing. This has led to more stringent regulations for aircraft noise (Casalino *et al.* 2008). With regard to the impact of aircraft on community noise, the take-off and landing process are of main concern. Among the different mechanisms present during the landing process, airframe noise is believed to be the dominant component. It is widely accepted that the broadband noise, induced by the interaction of boundary layer with the aerofoil trailing-edge, known as the turbulent boundary layer trailing-edge noise, plays a significant role in the overall airframe noise. Turbulent boundary layer trailing-edge noise also dominates the noise produced by wind turbines (Oerlemans *et al.* 2007). Unless explicitly stated, the turbulent boundary layer trailing-edge noise will be referred to as trailing-edge noise in the rest of this paper.

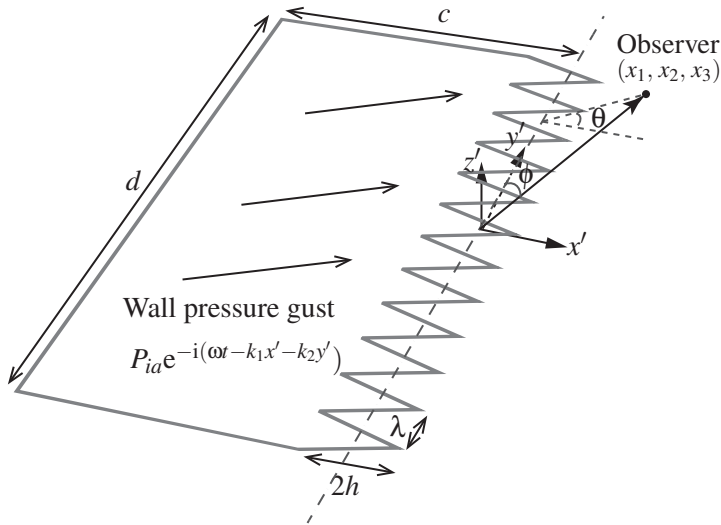† Email address for correspondence: m.azarpeyvand@bristol.ac.uk

FIGURE 1. The schematic of a flat plate with and trailing-edge serrations.

When a turbulent boundary layer convects past the trailing-edge, unsteady pressure with a wavenumber in the hydrodynamic range is scattered into sound (Chase 1975). Both experiments and theory reveal that the radiated sound power varies with the flow velocity to the power of 5, which is more efficient, at low Mach numbers, compared to the power of 8 valid for free stream flows (Lighthill 1952; Williams & Hall 1970).

Different models have been put forward for predicting and understanding trailing-edge noise. In 1976, Amiet (1976b, 1978) proposed a semi-analytical model in which the aerofoil is modelled as a flat plate. The model followed Schwarzschild's technique to obtain the scattered pressure on the surface of the flat plate and the far-field sound was obtained using the surface pressure integral based on the theories of Kirchoff and Curle. The model established an analytical relationship between the far-field sound spectral density and the wavenumber spectral density of the wall surface pressure under the turbulent boundary layer. Amiet's model agrees well with experimental observations, especially at high frequencies (Roger & Moreau 2005). Note that Amiet's model assumed that the leading edge of the plate is infinitely far away from the trailing-edge and thus has no effects on the scattered pressure, which might not be accurate at low frequencies. In 2005, in order to investigate the leading-edge back-scattering effects, Roger & Moreau (2005) extended Amiet's model by incorporating the back-scattered pressure from the leading edge and found that when the Helmholtz number $kc > 1$, the back-scattering can be safely ignored and only at very low frequencies does the back-scattering alter the far-field sound.

As trailing-edge noise dominates the sound generation at low Mach numbers, different noise reduction techniques have been investigated. Howe proposed a theoretical model to predict the sound generated by a semi-infinite plate with serrated trailing-edge of sinusoidal and sawtooth profiles (Howe 1991a,b), see figure 1. Howe's models show that sawtooth serrations are more effective in reducing the trailing-edge noise than the sinusoidal ones and that the use of sharp sawtooth serrations, i.e. $2h/\lambda > 8$, can lead to significant reduction of trailing-edge noise. More recently, Azarpeyvand *et al.* (2013) carried out an analytical investigation of trailing-edge noise reduction using novel serrations, namely, sawtooth, sinusoidal, slitted, slitted-sawtooth and sawtooth-sinusoidal. It has been found that the noise reduction is a sensitive function of the complexity of the

serration geometry and significant noise reduction can be achieved by applying complex periodic serrations to the trailing-edge. It has also been shown that the slitted-sawtooth serration is the most effective design amongst the aforementioned serration geometries.

An experimental investigation on trailing-edge serrations was performed by Dassen *et al.* (1996). Both aerofoils and flat plates of different shapes were tested in a wind tunnel. A maximum of 10 dB noise reduction for the flat plate and 8 dB reduction for the aerofoils were reported, both of which occurred mainly at low frequencies. Later, Parchen *et al.* (1999) conducted an experimental investigation of the aeroacoustic effects of trailing-edge serrations on wind turbine blades at both full and wind-tunnel scales. An average sound reduction slightly below that reported by Dassen *et al.* was observed. Most recently, Oerlemans *et al.* (2009) examined and compared the noise generated by standard, serrated and aeroacoustically-optimized aerofoils, but only 2-3 dB noise reduction was achieved for the aerofoil with serrated trailing-edge at low frequencies. Both Parchen *et al.* (1999) and Oerlemans *et al.* (2009) reported a noise increase at high frequencies.

Gruber (2012) recently conducted an extensive experimental investigation on the aeroacoustic performance of aerofoils fitted with different sawtooth and novel serrations. The acoustic measurements were performed to give the sound power level (SWL) integrated in the mid-span plane. An average of 3-5 dB reduction was achieved using sharp sawtooth serrations, and a noise increase of up to 5 dB at higher frequencies was also reported. It was explained that the significant reduction of phase speed near the sawtooth edges, together with a slight reduction of the coherence of pressure measured along the edge is responsible for the sound reduction observed in experiments. All the experimental studies, however, indicate that Howe's model significantly overpredicts the sound reduction capability of trailing-edge serrations. This might be caused by the assumptions and approximations used in Howe's derivation, which will be discussed in detail in the subsequent sections.

Although different serrations have been used in many applications such as wind turbines and jet nozzles (Oerlemans *et al.* 2009; Callender *et al.* 2005; Yan *et al.* 2007), the physical mechanism of the noise reduction remains poorly understood. Howe's model gave a first insight into the physics involved, but the large deviation from experiments suggests a new and more accurate theory is needed.

The main objectives of this paper are to develop a new theory to predict the sound generated from a serrated trailing-edge more accurately, and to improve our understanding of the sound reduction mechanism due to the presence of trailing-edge serrations. The paper is structured as follows: the new theoretical model for sound radiation from serrated trailing-edges is presented in Sec. 2. Section 3 provides validation results against finite element solution. A parametric study will also be presented and the effects of serrations on trailing-edge noise directivity will also be discussed. A comparison between the new model and Howe's model is made in Sec. 4. The physical mechanism of sound reduction using trailing-edge serrations is discussed in Sec. 5 and noise reduction criteria developed based on the results in Sec. 2 will be listed and discussed. A brief conclusion is given in the last section.

2. Analytical formulation

As for Amiet's model, the analytical model developed here is based on Schwarzschild's technique for the Helmholtz equation with a discontinuous boundary condition. It is therefore useful to begin with describing this technique. The Schwarzschild method (Amiet

1976*b*; Roger & Moreau 2005) states that if a function $f(x, y)$ satisfies

$$
\begin{cases}
\dfrac{\partial^2 f}{\partial x^2} + \dfrac{\partial^2 f}{\partial y^2} + \mu^2 f = 0 \\[2mm]
\dfrac{\partial f}{\partial y}(x, 0) = 0, & x < 0 \\[2mm]
f(x, 0) = g(x), & x \geqslant 0,
\end{cases}
\tag{2.1}
$$

then, for $x < 0$,

$$
f(x, 0) = \frac{1}{\pi} \int_0^\infty \sqrt{\frac{-x}{\xi}} \frac{\mathrm{e}^{\mathrm{i}\mu(\xi - x)}}{\xi - x} g(\xi) \, \mathrm{d}\xi.
\tag{2.2}
$$

As shown by Amiet (1976*a*), the above method can be used to obtain the scattered pressure field over the surface of the aerofoil.

2.1. *The mathematical model*

Consider an aerofoil with trailing-edge serrations, modelled as a flat plate as shown in figure 1, with an infinitesimal thickness and an averaged chord length c and spanwise length d. Let x', y' and z' denote the streamwise, spanwise and normal to the plate coordinates, respectively. The observer point is located at (x_1, x_2, x_3). The profile function $H(y')$ is used to describe the serrated edges. The origin of the coordinates is chosen in such a way that $H(y')$ is an oscillatory function of zero mean and that $H(y') = 0$ in the absence of serrations. Figure 1 shows a sawtooth serration with a root-to-tip amplitude of $2h$ and a wavelength of λ.

When the sound wavelength is equal to or shorter than the chord length c, the flat plate can be treated as a semi-infinite plate without a leading-edge (Amiet 1976*b*). Furthermore, the plate can be considered infinite in the spanwise direction provided it has a relatively large aspect ratio (typically $d/c > 3$) (Amiet 1978; Roger & Carazo 2010) . The turbulence inside the boundary layer is assumed to be frozen, i.e. it remains statistically the same before and after passing over the trailing-edge.

After implementing a spatial and time Fourier transformation, the hypothetical surface pressure beneath the turbulent boundary layer that would exist when the flat plate is infinite can be expressed as an integral of different wall pressure gust components. The incoming wall pressure gust of frequency ω , as illustrated in figure 1, takes the form of

$$
p_i = P_i \mathrm{e}^{-\mathrm{i}(\omega t - k_1 x' - k_2 y')},
\tag{2.3}
$$

where P_i is the magnitude of the incident wall pressure gust and k_1 and k_2 denote the wavenumbers in the chordwise and spanwise directions, respectively.

The sound sources due to the presence of solid boundaries (Curle 1955) can be modelled as dipoles, in addition to the quadrupoles in free field (Lighthill 1952). As explained in Amiet's paper (Amiet 1976*b*), the incident pressure produces a scattered field originating from the trailing-edge, due to the change in boundary condition at the wall. The scattered field induces a pressure jump that cancels the incident pressure jump at the trailing-edge and in the wake after the plate (Kutta condition). Thus, the total pressure can be decomposed into two parts, namely $p_t = p_i + p$. The incident wall pressure is given by (2.3) and the scattered pressure field, p, must satisfy the following conditions at $z' = 0$,

$$
\begin{cases}
\dfrac{\partial p}{\partial z'} = 0, & x' < H(y') \\[2mm]
p = -P_i \mathrm{e}^{-\mathrm{i}(\omega t - k_1 x' - k_2 y')}, & x' \geqslant H(y').
\end{cases}
\tag{2.4}
$$

It is worth pointing out that the incident pressure p_i defined in (2.3) is twice the "con-

ventional incident pressure" that would exist when the semi-infinite flat plate is absent. Therefore the scattered pressure p to be obtained on the upper surface of the plate would be twice the "conventional scattered pressure" due to the linearity of wave equation and (2.4). Since the scattering problem is anti-symmetrical, it follows that the scattered pressure p is in fact, as in Amiet's paper (Amiet 1976b), the scattered pressure jump across the plate. This can be made evident through a more rigorous analysis.

In the plate-fixed frame $\{x', y', z'\}$, the air flow has a uniform speed U in the streamwise direction outside the boundary layer and the wave equation governing the scattered pressure field p is

$$\nabla^2 p - \frac{1}{c_0^2}\left(\frac{\partial}{\partial t} + U\frac{\partial}{\partial x'}\right)^2 p = 0, \tag{2.5}$$

where c_0 denotes the speed of sound. With the assumption of harmonic perturbation $p = P(x', y', z')\mathrm{e}^{-\mathrm{i}\omega t}$, the above equation reduces to

$$\beta^2\frac{\partial^2 P}{\partial x'^2} + \frac{\partial^2 P}{\partial y'^2} + \frac{\partial^2 P}{\partial z'^2} + 2\mathrm{i}kM_0\frac{\partial P}{\partial x'} + k^2 P = 0, \tag{2.6}$$

where $k = \omega/c_0$, $\beta^2 = 1 - M_0^2$ and $M_0 = U/c_0$.

In order to make the boundary conditions in (2.4) independent of y', the coordinate transformation (Roger *et al.* 2013) $x = x' - H(y')$, $y = y'$, $z = z'$ is used and leads to the following differential equation:

$$\left(\beta^2 + H'^2(y)\right)\frac{\partial^2 P}{\partial x^2} + \frac{\partial^2 P}{\partial y^2} + \frac{\partial^2 P}{\partial z^2} - 2H'(y)\frac{\partial^2 P}{\partial x\partial y} + (2\mathrm{i}M_0 k - H''(y))\frac{\partial P}{\partial x} + k^2 P = 0, \tag{2.7}$$

where $H'(y)$ and $H''(y)$ denote the first and second derivatives of $H(y)$. The boundary conditions now read

$$\begin{cases} P(x, y, 0) = -P_i\mathrm{e}^{\mathrm{i}(k_1 x + k_2 y)}\mathrm{e}^{\mathrm{i}k_1 H(y)}, & x \geqslant 0 \\ \partial P(x, y, 0)/\partial z = 0, & x < 0. \end{cases} \tag{2.8}$$

Since the coefficients in (2.7) are y-dependent, the standard "separation of variables" technique cannot be applied to solve this equation. We therefore turn to using a Fourier expansion technique in the following derivation.

2.2. *Fourier expansion*

As the scattering problem is periodic in the spanwise direction, one can expand the scattered pressure field using Fourier series as

$$P(x, y, z) = \sum_{-\infty}^{\infty} P_n(x, z)\mathrm{e}^{\mathrm{i}k_{2n} y}, \tag{2.9}$$

where $k_{2n} = k_2 + 2n\pi/\lambda$.

Substituting the above expression into the transformed wave equation, shown in (2.7), yields

$$\left\{\left(\beta^2 + H'^2(y)\right)\frac{\partial^2}{\partial x^2} + \frac{\partial^2}{\partial y^2} + \frac{\partial^2}{\partial z^2} - 2H'(y)\frac{\partial^2}{\partial x\partial y} + (2\mathrm{i}M_0 k - H''(y))\frac{\partial}{\partial x} + k^2\right\}$$
$$\sum_{-\infty}^{\infty} P_n(x, z)\mathrm{e}^{\mathrm{i}k_{2n} y} = 0. \tag{2.10}$$

Multiplying (2.10) by $\mathrm{e}^{-\mathrm{i}k_{2n'} y}$, then integrating it over y from $-\lambda/2$ to $\lambda/2$, it can be
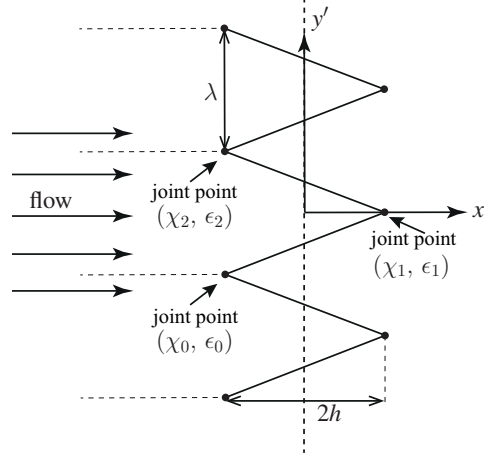
FIGURE 2. The schematic of sawtooth serrations.

readily shown that

$$\left\{\beta^2\frac{\partial^2}{\partial x^2} + \frac{\partial^2}{\partial z^2} + 2\mathrm{i}kM_0\frac{\partial}{\partial x} + (k^2 - k_{2n'}^2)\right\} P_{n'}(x,z)+$$

$$\frac{1}{\lambda}\int_{-\lambda/2}^{\lambda/2}\sum_{n=-\infty}^{\infty}\left\{H'^2(y)\frac{\partial^2}{\partial x^2} - (H''(y) + 2\mathrm{i}k_{2n}H'(y))\frac{\partial}{\partial x}\right\} P_n(x,z)\mathrm{e}^{\mathrm{i}[2(n-n')\pi/\lambda]y}\,\mathrm{d}y = 0.$$

$$(2.11)$$

Note that when both $H'(y)$ and $H''(y)$ are constant within an entire sawtooth wave-length, the summation over different modes in (2.11) can be dropped and we obtain a fully decoupled differential equation for mode n'. However, this means that the flat plate has a straight or swept trailing-edge. For serrations of an arbitrary profile, both $H'(y)$ and $H''(y)$ generally depend on y. Thus 2.11 becomes a coupled differential equation, i.e. more than one mode appears in each differential equation. The physical interpretation of this mode coupling will be discussed later.

In this paper, we only focus on the sawtooth serration, which has been shown to be effective in reducing the trailing-edge noise Howe (1991b). The method can however also be used for other serrations. Consider a sawtooth centred around the coordinate origin, and let (χ_0, ϵ_0), (χ_1, ϵ_1) and (χ_2, ϵ_2) be the Cartesian coordinates of the tip and roots of the sawtooth, as shown in figure 2. The serration profile function $H(y)$ can therefore be defined as

$$H(y) = \begin{cases} \sigma_0(y - \chi_0 - m\lambda) + \epsilon_0, & \chi_0 + m\lambda < y \leqslant \chi_1 + m\lambda \\ \sigma_1(y - \chi_1 - m\lambda) + \epsilon_1, & \chi_1 + m\lambda < y \leqslant \chi_2 + m\lambda, \end{cases} \quad (2.12)$$

where $\sigma_j = (\epsilon_{j+1} - \epsilon_j)/(\chi_{j+1} - \chi_j)$, $j = 0, 1$ and $m = 0, \pm 1, \pm 2, \pm 3 \cdots$. Let σ, defined as $\sigma = |\sigma_j| = 4h/\lambda$, denote the sharpness of the sawtooth serrations. For a sawtooth profile, as mentioned above, $H'(y)$ is not continuous and $H''(y)$ is thus singular at the joint-points. We use the conventional generalized function $\delta(x)$ to describe the singularities at

these points, i.e.

$$H'(y) = \begin{cases} \sigma_0, & \chi_0 + m\lambda < y \leqslant \chi_1 + m\lambda \\ \sigma_1, & \chi_1 + m\lambda < y \leqslant \chi_2 + m\lambda \end{cases}$$

$$H''(y) = \sum_{m=-\infty}^{\infty} (-1)^{m+1} 2\sigma \delta(y - m\lambda/2). \tag{2.13}$$

Substituting the serration profile function and its derivatives, (2.12) and (2.13), into the wave equation, (2.11), and making use of the fact that $\int_{-\infty}^{\infty} f(x)\delta(x - \tau)\,\mathrm{d}x = f(\tau)$, we obtain

$$\left\{ (\beta^2 + \sigma^2) \frac{\partial^2}{\partial x^2} + \frac{\partial^2}{\partial z^2} + 2\mathrm{i}kM_0 \frac{\partial}{\partial x} + (k^2 - k_{2n'}^2) \right\} P_{n'}(x, z)$$
$$= -\frac{4\sigma}{\lambda} \sum_{n-n'=odd} \left(1 - \frac{k_2\lambda + 2n\pi}{(n - n')\pi} \right) \frac{\partial P_n(x, z)}{\partial x}. \tag{2.14}$$

To make the above equation more compact, we write the set of differential equations obtained above into a matrix form. Let a linear operator

$$\mathrm{D} = \left\{ (\beta^2 + \sigma^2) \frac{\partial^2}{\partial x^2} + \frac{\partial^2}{\partial z^2} + 2\mathrm{i}kM_0 \frac{\partial}{\partial x} \right\}, \tag{2.15}$$

and a vector of functions

$$\boldsymbol{P} = (\cdots P_{-n'}(x, z),\ P_{-n'+1}(x, z),\ \cdots P_{n'-1}(x, z),\ P_{n'}(x, z),\ \cdots)^T, \tag{2.16}$$

then the coupled equations can be written as

$$\mathrm{D}\boldsymbol{P} - A\boldsymbol{P} = B\frac{\partial \boldsymbol{P}}{\partial x}, \tag{2.17}$$

where the symbol T in (2.16) represents the transpose of a matrix. Matrices A and B denote the coefficient matrices of $\boldsymbol{P}$ and $\partial \boldsymbol{P}/\partial x$, respectively. A_{ml} and B_{ml} representing the entry corresponding to mode m in row and l in column of matrices A and B are

$$A_{ml} = (k_{2m}^2 - k^2)\delta_{ml}, \quad B_{ml} = \begin{cases} \dfrac{4\sigma}{\lambda} \dfrac{m + l + k_2\lambda/\pi}{l - m}, & m - l \text{ is odd} \\ 0, & m - l \text{ is even,} \end{cases} \tag{2.18}$$

where δ_{ml} represents the Kronecker delta. Note that the index of matrices A and B are from $-m$ to m and $-l$ to l rather than from 1 to $2m + 1$ and 1 to $2l + 1$ given the fact that the mode number are symmetric with respect to 0.

Substituting the profile geometry, (2.12), into the boundary conditions, (2.8), and performing the same Fourier expansions, yields

$$\begin{cases} P_n(x, 0) = -P_i a_n \mathrm{e}^{\mathrm{i}k_1 x}, & x > 0 \\ \dfrac{\partial P_n}{\partial z}(x, 0) = 0, & x \leqslant 0, \end{cases} \tag{2.19}$$

where a_n are defined as

$$a_n = \frac{1}{\lambda} \int_{-\lambda/2}^{\lambda/2} \mathrm{e}^{\mathrm{i}k_1 H(y)} \mathrm{e}^{-\mathrm{i}2n\pi y/\lambda}\,\mathrm{d}y. \tag{2.20}$$

In (2.17), as B is not a diagonal matrix, the term $B(\partial \boldsymbol{P}/\partial x)$ contains coupling terms, in the sense that different modes, P_n for example, appear in the governing equation

of P_m. This means that every mode is interacting with the other modes and cannot be solved independently. From the expression of B in (2.18), it can be seen that the strength of coupling is proportional to σ/λ. This indicates that sharper serrations have stronger coupling between different modes. Also note that A is a diagonal matrix, so if $B \approx 0$, i.e. the serrations are very wide, then there is no coupling effect and one can solve each mode independently.

At very low frequencies, the contribution of higher modes is expected to become gradually negligible compared to mode 0. Thus, it can be reasonably assumed that in the case of the governing equation of P_0 (mode 0), the coupling with higher modes is weak and one can solve P_0 individually. The coupling effect becomes more pronounced at high frequencies and for sharp serrations. To solve these coupled equations at relatively high frequencies, one can use an iterative procedure, to be introduced in the next section.

2.3. *The iterative solution procedure*

2.3.1. *Scattered surface pressure*

To obtain the scattered surface pressure, equation (2.17) together with the boundary conditions in (2.19) need to be solved. By analogy with the solution of a system of linear algebraic equation (Süli & Mayers 2003), which can be obtained iteratively, we shall solve our system of PDEs in an iterative manner.

Substituting a known initial value $\boldsymbol{P}^{(0)}$ into the coupling term in (2.17), one can write

$$\mathrm{D}\boldsymbol{P} - A\boldsymbol{P} = B\frac{\partial \boldsymbol{P}^{(0)}}{\partial x}. \tag{2.21}$$

Solving (2.21) yields a new set of solutions $\boldsymbol{P}^{(1)}$. Replacing $\boldsymbol{P}^{(0)}$ in (2.21) with $\boldsymbol{P}^{(1)}$, we obtain a new wave equation,

$$\mathrm{D}\boldsymbol{P} - A\boldsymbol{P} = B\frac{\partial \boldsymbol{P}^{(1)}}{\partial x}. \tag{2.22}$$

Solving (2.22) gives a new set of solutions $\boldsymbol{P}^{(2)}$. This process is repeated to obtain a solution sequence, $\boldsymbol{P}^{(0)}$, $\boldsymbol{P}^{(1)}$, $\boldsymbol{P}^{(2)}$, $\boldsymbol{P}^{(3)} \cdots$. If the sequence is convergent, then its limit satisfies (2.17).

The initial value $\boldsymbol{P}^{(0)}$ used to start the first iteration can be obtained, as mentioned in the previous section, by ignoring all the coupling terms, i.e. with $B = 0$, and by solving each equation individually via the standard Schwarzschild technique, as shown in (2.2). The solution to each equation in the decoupled system of equations

$$\mathrm{D}\boldsymbol{P} - A\boldsymbol{P} = 0 \tag{2.23}$$

can be found as follows.

After use is made of the transformation of $P_{n'} = \bar{P}_{n'}\mathrm{e}^{-\mathrm{i}kM_0x/(\beta^2+\sigma^2)}$, individual equations in (2.23) reduce to,

$$\{(\beta^2 + \sigma^2)\frac{\partial^2}{\partial x^2} + \frac{\partial^2}{\partial z^2} + K_{n'}^2(\beta^2 + \sigma^2)\}\bar{P}_{n'} = 0, \tag{2.24}$$

where

$$K_{n'} = \sqrt{k^2(1 + \sigma^2) - k_{2n'}^2(\beta^2 + \sigma^2)}/(\beta^2 + \sigma^2). \tag{2.25}$$

Making use of $X = x, Z = \sqrt{\beta^2 + \sigma^2}z$, one can show that (2.24) reduces to a standard Schwarzschild problem and the solution can be found using the Schwarzschild integral

described in (2.2), as

$$P_{n'}^{(0)} = P_i \mathrm{e}^{\mathrm{i}k_1 x} a_{n'} \big((1-\mathrm{i})\mathrm{E}(-\mu_{n'} x) - 1 \big), \tag{2.26}$$

where $P_{n'}^{(0)}$ is the element of the vector $\boldsymbol{P}^{(0)}$ corresponding to the n'-th mode, and

$$\mu_{n'} = K_{n'} + k_1 + \frac{kM_0}{\beta^2 + \sigma^2},$$
$$\mathrm{E}(x) = \int_0^x \frac{\mathrm{e}^{\mathrm{i}t}}{\sqrt{2\pi t}} \,\mathrm{d}t. \tag{2.27}$$

The initial solutions obtained by ignoring all the coupling terms denote the decoupled part of the exact solution of each mode, which implies that the n-th mode excitation $(x > 0)$ produces only an n-th mode response $(x < 0)$. The iteration procedure will add a coupled part to the solution of each mode. The coupled part implies that an n-th mode input $(x > 0)$ will also produce some m-th mode responses $(x < 0)$, where $m \neq n$. It can be expected that those coupling contributions from closer modes are stronger than remote ones. For sawtooth serrations, as will be shown in (2.30), the coupling strength decays quadratically with respect to the difference between their "mode number", i.e. $|m - l|$.

By substituting $\boldsymbol{P}^{(0)}$ into the coupling terms on the right hand side of (2.17), one obtains some inhomogeneous equations that can no longer be solved using the standard Schwarzschild technique. However, if one can transform these equations into homogeneous ones, then Schwarzschild's method can again be applied. Note that $\boldsymbol{P}^{(0)}$ satisfies (2.23), hence, for $x \neq 0$, where $\boldsymbol{P}^{(0)}$ is first-order continuously differentiable, the following equation holds:

$$\mathrm{D}\frac{\partial \boldsymbol{P}^{(0)}}{\partial x} - A\frac{\partial \boldsymbol{P}^{(0)}}{\partial x} = 0. \tag{2.28}$$

Making use of (2.28), (2.21) can be equivalently written as

$$\mathrm{D}\left(\boldsymbol{P} + v\frac{\partial \boldsymbol{P}^{(0)}}{\partial x}\right) - A\left(\boldsymbol{P} + v\frac{\partial \boldsymbol{P}^{(0)}}{\partial x}\right) = 0, \tag{2.29}$$

where v is a coefficient matrix whose entries are

$$v_{ml} = \frac{B_{ml}}{k_{2m}^2 - k_{2l}^2} = \begin{cases} \dfrac{-4h}{\pi^2(m-l)^2}, & m - l = odd \\ 0, & m - l = even. \end{cases} \tag{2.30}$$

It is worth pointing out that (2.29) only holds when $x \in \mathbf{R}$ and $x \neq 0$, and in order to apply the Schwarzschild technique, it must be valid over the whole domain. However, since the singularity of $\partial \boldsymbol{P}^{(0)}/\partial x$ only exists at $x = 0$, similar to the differentiation of $H(y)$, we may again make use of the generalized function to account for this singularity. Let $\partial \hat{\boldsymbol{P}}^{(0)}/\partial x$ denote the generalized differentiation, which allows the presence of generalized functions at singular point $x = 0$ but equals to $\partial \boldsymbol{P}^{(0)}/\partial x$ elsewhere, then equation

$$\mathrm{D}\frac{\partial \hat{\boldsymbol{P}}^{(0)}}{\partial x} - A\frac{\partial \hat{\boldsymbol{P}}^{(0)}}{\partial x} = 0 \tag{2.31}$$

needs to hold over $x \in \mathbf{R}$. The Schwarzschild technique suggests that if (2.31) does hold, then the routine application of the steps described from (2.24) to (2.26) shall recover the value of $\partial \boldsymbol{P}^{(0)}/\partial x$ for $x < 0$. Thus, one can verify that the intended $\partial \hat{\boldsymbol{P}}^{(0)}/\partial x$ can indeed

be found as

$$\frac{\partial \hat{P}_{n'}^{(0)}}{\partial x}(x,0) = \frac{\partial P_{n'}^{(0)}}{\partial x}(x,0) + P_i a_{n'}(1-\mathrm{i})(-\sqrt{\mu_{n'}})\sqrt{2\pi x}\delta(x), \tag{2.32}$$

where $\partial \hat{P}_{n'}^{(0)}/\partial x$ denotes the element of $\partial \hat{\boldsymbol{P}}^{(0)}/\partial x$, corresponding to the n'-th mode and

$$\int_0^\infty \delta(x)\,\mathrm{d}x = \frac{1}{2}. \tag{2.33}$$

Now, the first iterated solution can be obtained by solving equation

$$\mathrm{D}\left(\boldsymbol{P} + v\frac{\partial \boldsymbol{P}^{(0)}}{\partial x}\right) - A\left(\boldsymbol{P} + v\frac{\partial \boldsymbol{P}^{(0)}}{\partial x}\right) = 0, \tag{2.34}$$

via the steps described from (2.24) to (2.26).

Solving (2.34) gives the values of $\boldsymbol{P}^{(1)}$. Continuing this iteration process gives $\boldsymbol{P}^{(2)}$, $\boldsymbol{P}^{(3)}\cdots$. The exact solutions $\boldsymbol{P}$ can also be expressed as

$$\boldsymbol{P}(x,0) = \boldsymbol{N}(x) + \boldsymbol{C}^{(1)}(x) + \boldsymbol{C}^{(2)}(x) + \boldsymbol{C}^{(3)}(x) + \cdots, \tag{2.35}$$

where $\boldsymbol{N}$ is the non-coupled part and the coupled parts are denoted by $\boldsymbol{C}^{(i)} = \boldsymbol{P}^{(i)} - \boldsymbol{P}^{(i-1)}$ ($i = 1,2,3\cdots$). The entries of $\boldsymbol{N}$ and $\boldsymbol{C}^{(1)}$ corresponding to mode n' are given by

$$N_{n'}(x) = P_i\mathrm{e}^{\mathrm{i}k_1 x}a_{n'}\left((1-\mathrm{i})\mathrm{E}(-\mu_{n'}x) - 1\right), \tag{2.36}$$

$$C_{n'}^{(1)}(x) = P_i\mathrm{e}^{\mathrm{i}k_1 x}(1-\mathrm{i})\sum_{m=-\infty}^{\infty} v_{n'm}a_m\left(\mathrm{i}k_1\left(\mathrm{E}(-\mu_{n'}x) - \mathrm{E}(-\mu_m x)\right)\right.$$
$$\left. -\sqrt{\frac{\mu_m}{-2\pi x}}\left(\mathrm{e}^{-\mathrm{i}\mu_{n'}x} - \mathrm{e}^{-\mathrm{i}\mu_m x}\right)\right). \tag{2.37}$$

The elements of the second-order function $\boldsymbol{C}^{(2)}$ are provided in appendix A. Since $v_{ml} \propto h$ it can be readily shown that $C_{n'}^{(i)} \propto h^i$ for $i = 1, 2, 3\cdots$. This means that the solution presented in (2.35) is a perturbation (Taylor-expansion) series with respect to half of the root-to-tip amplitude h. Therefore a smaller value of h compared to the sound wavelength yields faster convergence. Note that the function $\boldsymbol{C}^{(i)}$ becomes more and more complex as i increases. However, if $\boldsymbol{C}^{(i)}$ vanishes sufficiently quickly, higher orders can be neglected without causing significant errors. This appears to be the case for the frequencies relevant to trailing-edge noise, see Sec. 3.2. Substituting (2.36), (2.37) and (A 2) into (2.35), a second-order approximation of the exact solutions is obtained.

The scattered surface pressure is obtained by summing $P_{n'}(x,0)$ over all different modes and transforming back to the physical coordinate system, namely

$$P(x',y',0) = \sum_{n'=-\infty}^{\infty} P_{n'}(x' - H(y'),0)\mathrm{e}^{\mathrm{i}k_{2n'}y'}. \tag{2.38}$$

Here, $P_{n'}$ is the solution obtained from the iteration procedure mentioned above,

$$P(x',y',0) = \sum_{n'=-\infty}^{\infty} (N_{n'} + C_{n'}^{(1)} + C_{n'}^{(2)} + \cdots)(x' - H(y'),0)\mathrm{e}^{\mathrm{i}k_{2n'}y'}, \tag{2.39}$$

where $N_{n'}$ and $C_{n'}^{(1)}$ are defined in (2.36) and (2.37), and $C_{n'}^{(2)}$ can be found in appendix A. Note that the terms in the second parenthesis are the arguments for the $N_{n'}$ and

$C_{n'}^{(i)}$ $(i = 1, 2, 3, \cdots)$ functions. It is worth pointing out that in the limiting case when $H(y') = 0$, $\boldsymbol{C}^{(i)}$ vanishes, and (2.39) reduces to the result obtained by Amiet (1976b) for a straight edge.

As shown in (2.39), the scattered pressure field can now be expressed in terms of an infinite series. By inspection of (2.39), one can show that at sufficiently low frequencies, i.e. $k_1 h < \pi^2/4$, the infinite series is absolutely convergent. At higher frequencies, the series still appears to be convergent, but to obtain satisfactory approximation, a higher truncation number and higher-order iterations may be required. The convergence of the series will be discussed in the following sections by comparing the far-field sound predicted using different order approximations.

2.3.2. *Far-field sound pressure*

As illustrated in figure 1, the observer point is located at (x_1, x_2, x_3) and the flat plate has an averaged chord length c and span length d. The far field sound can be found using the surface pressure integral as mentioned in Amiet's model (Lamb 1932; Curle 1955; Amiet 1975):

$$p_f(\mathbf{x}, \omega) = \frac{-\mathrm{i}\omega x_3}{4\pi c_0 S_0^2} \iint_s \Delta P(x', y') \mathrm{e}^{-\mathrm{i}kR} \,\mathrm{d}x' \,\mathrm{d}y', \qquad (2.40)$$

where $\Delta P = P$ denotes the pressure jump, and $S_0^2 = x_1^2 + \beta^2(x_2^2 + x_3^2)$ and

$$R = \frac{M_0(x_1 - x') - S_0}{\beta^2} + \frac{x_1 x' + x_2 y' \beta^2}{\beta^2 S_0}. \qquad (2.41)$$

By substituting the solution obtained in (2.39) into (2.40), the far-field sound pressure can be expressed as

$$p_f(\mathbf{x}, \omega, k_2) = P_i \left(\frac{-\mathrm{i}\omega x_3 c}{4\pi c_0 S_0^2} \right) \lambda \frac{\sin\left((N + 1/2)\lambda(k_2 - kx_2/S_0)\right)}{\sin\left((k_2 - kx_2/S_0)\lambda/2\right)} \mathcal{L}(\omega, k_1, k_2). \qquad (2.42)$$

Here, $2N + 1$ represents the number of sawteeth on the edge and the far-field sound gust-response function $\mathcal{L}$ is defined as

$$\mathcal{L}(\omega, k_1, k_2) = (1 - \mathrm{i}) \frac{1}{\lambda c} \mathrm{e}^{-\mathrm{i}k(M_0 x_1 - S_0)/\beta^2} \mathrm{e}^{\mathrm{i}k(M_0 - x_1/S_0)h/\beta^2}$$
$$\sum_{n'=-\infty}^{\infty} \left(\Theta_{n'} + \Theta_{n'}^{(1)} + \Theta_{n'}^{(2)} + \cdots \right), \qquad (2.43)$$

with (only the first two terms are given, see more results in appendix A)

$$\Theta_{n'} = a_{n'} Q_{n'n'},$$
$$\Theta_{n'}^{(1)} = \sum_{m=-\infty}^{\infty} v_{n'm} \mathrm{i}k_1 a_m (Q_{n'n'} - Q_{n'm}) - v_{n'm} \sqrt{\mu_m} a_m (S_{n'n'} - S_{n'm}). \qquad (2.44)$$

The functions Q_{nm} and S_{nm} in the above equations are given by

$$Q_{nm} = \sum_{j=0}^{1} \frac{1}{\kappa_{nj}} \left(\frac{1}{\mu_A} \left(\mathrm{e}^{\mathrm{i}\kappa_{nj}\chi_{j+1}} \Gamma(c + \epsilon_{j+1}; \mu_m, \mu_A) - \mathrm{e}^{\mathrm{i}\kappa_{nj}\chi_j} \Gamma(c + \epsilon_j; \mu_m, \mu_A) \right) \right.$$
$$\left. - \frac{1}{\mu_{Bnj}} \mathrm{e}^{\mathrm{i}\kappa_{nj}(\chi_j - (c+\epsilon_j)/\sigma_j)} \left(\Gamma(c + \epsilon_{j+1}; \mu_m, \mu_{Bnj}) - \Gamma(c + \epsilon_j; \mu_m, \mu_{Bnj}) \right) \right), \qquad (2.45)$$

$$S_{nm} = \sum_{j=0}^{1} \frac{1}{\mathrm{i}\kappa_{nj}} \Big(\frac{1}{\sqrt{\eta_{Am}}} \big(\mathrm{e}^{\mathrm{i}\kappa_{nj}\chi_{j+1}} \mathrm{E}(\eta_{Am}(c+\epsilon_{j+1})) - \mathrm{e}^{\mathrm{i}\kappa_{nj}\chi_j} \mathrm{E}(\eta_{Am}(c+\epsilon_j)) \big) \big)$$
$$- \frac{1}{\sqrt{\eta_{Bmj}}} \mathrm{e}^{\mathrm{i}\kappa_{nj}(\chi_j - (c+\epsilon_j)/\sigma_j)} \big(\mathrm{E}(\eta_{Bmj}(c+\epsilon_{j+1})) - \mathrm{E}(\eta_{Bmj}(c+\epsilon_j)) \big) \Big),$$

where the function Γ is defined by

$$\Gamma(x;\mu,\nu) = \mathrm{e}^{-\mathrm{i}\nu x} \mathrm{E}(\mu x) - \sqrt{\frac{\mu}{\mu-\nu}} \mathrm{E}((\mu-\nu)x) + \frac{1}{1-\mathrm{i}}(1-\mathrm{e}^{-\mathrm{i}\nu x}), \qquad (2.46)$$

and

$$\begin{aligned}
\mu_A &= k_1 + k(M_0 - x_1/S_0)/\beta^2, \\
\mu_{Bnj} &= k_1 - (k_{2n} - kx_2/S_0)/\sigma_j, \\
\kappa_{nj} &= k_{2n} - kx_2/S_0 + k(M_0 - x_1/S_0)\sigma_j/\beta^2, \\
\eta_{Am} &= K_m + kM_0/(\beta^2 + \sigma^2) - k(M_0 - x_1/S_0)/\beta^2, \\
\eta_{Bmj} &= K_m + kM_0/(\beta^2 + \sigma^2) + (k_{2n} - kx_2/S_0)/\sigma_j.
\end{aligned} \qquad (2.47)$$

Note that (2.42) is the far-field sound induced by the scattered pressure only. When the incident pressure is also incorporated, as pointed out by Amiet (1978), the number 1 appearing in the parenthesis of function Γ should be omitted, i.e. the third term on the right hand side of (2.46) should be replaced by $-\mathrm{e}^{-\mathrm{i}\nu x}/(1-\mathrm{i})$.

2.3.3. *Statistical formulation*

The hypothetical surface pressure of frequency ω beneath a turbulent boundary layer on the plate surface that would exist when the plate is infinite can be expressed as a Fourier integral,

$$P_{int}(\omega, x', y') = \iint \widetilde{P}_{int}(\omega, k_1, k_2) \mathrm{e}^{\mathrm{i}(k_1 x' + k_2 y')} \, \mathrm{d}k_1 \, \mathrm{d}k_2. \qquad (2.48)$$

Generally, for a given frequency ω, k_1 can have different values (Amiet 1976*b*). However, experiments (Willmarth 1959) have shown that $P_i(\omega, k_1, k_2)$ peaks in the vicinity of $k_1 = \omega/U_c$, where U_c denotes the convection velocity of the wall pressure gusts and is only a weak function of ω. Hence upon defining $P_i(\omega, k_2) = \int_{-\infty}^{\infty} \widetilde{P}_{int}(\omega, k_1, k_2) \, \mathrm{d}k_1$, (2.48) reduces to

$$P_{int}(\omega, x', y') = \int_{-\infty}^{\infty} P_i(\omega, k_2) \mathrm{e}^{\mathrm{i}(\bar{k}_1 x' + k_2 y')} \, \mathrm{d}k_2, \qquad (2.49)$$

where $\bar{k}_1 = \omega/U_c$.

As shown in the preceding section, a wall pressure gust of

$$P_i(\omega, k_2) \mathrm{e}^{\mathrm{i}(k_1 x' + k_2 y')}$$

will induce a far-field sound pressure

$$\left(\frac{-\mathrm{i}\omega x_3 c}{4\pi c_0 S_0^2} \right) \lambda \frac{\sin\big((N+1/2)\lambda(k_2 - kx_2/S_0)\big)}{\sin\big((k_2 - kx_2/S_0)\lambda/2\big)} \mathcal{L}(\omega, k_1, k_2) P_i(\omega, k_2). \qquad (2.50)$$

Thus, the wall pressure defined by (2.49) will induce a far-field sound pressure of

$$p_f(\mathbf{x}, \omega) = \left(\frac{-\mathrm{i}\omega x_3 c}{4\pi c_0 S_0^2} \right) \int_{-\infty}^{\infty} \lambda \frac{\sin\left((N+1/2)\lambda(k_2 - k x_2/S_0)\right)}{\sin\left((k_2 - k x_2/S_0)\lambda/2\right)} \mathcal{L}(\omega, \bar{k}_1, k_2) P_i(\omega, k_2) \, \mathrm{d}k_2. \tag{2.51}$$

The PSD of the far-field sound is given by

$$S_{pp}(\mathbf{x}, \omega) = \lim_{T \to \infty} \left(\frac{\pi}{T} \langle p_f(\mathbf{x}, \omega) p_f^*(\mathbf{x}, \omega) \rangle \right), \tag{2.52}$$

where the asterisk denotes complex conjugate, and $2T$ is the time length used to obtain $p_f(\mathbf{x}, \omega)$ by performing Fourier transformation. Substituting (2.51) into (2.52) yields

$$S_{pp}(\mathbf{x}, \omega) = \left(\frac{\omega x_3 c}{4\pi c_0 S_0^2} \right)^2 \int_{-\infty}^{\infty} \lambda^2 \left(\frac{\sin\left((N+1/2)\lambda(k_2 - k x_2/S_0)\right)}{\sin\left((k_2 - k x_2/S_0)\lambda/2\right)} \right)^2 |\mathcal{L}|^2 \, \Pi(\omega, k_2) \, \mathrm{d}k_2, \tag{2.53}$$

where $\Pi(\omega, k_2)$ is the wavenumber spectral density (Amiet 1975) of the hypothetical wall pressure beneath the turbulent boundary layer on the plate surface. For very wide serrations, i.e. $h \approx 0$, (2.53) reduces to Amiet's model (Amiet 1976b). Equation (2.53) can be simplified by assuming a very large span, i.e. the number of serrations $(2N+1)$ is sufficiently large. Using the following equation,

$$\lim_{N \to \infty} \lambda^2 \frac{\sin^2\left((N+1/2)\lambda(k_2 - k x_2/S_0)\right)}{\sin^2\left((k_2 - k x_2/S_0)\lambda/2\right)} \sim 2\pi d \sum_{m=-\infty}^{\infty} \delta(k_2 - k x_2/S_0 + 2m\pi/\lambda), \tag{2.54}$$

where $\delta(x)$ is the conventional generalized function defined in Sec. 2, one can show that the PSD of the far-field sound in the plane $y' = 0$ is given by

$$S_{pp}(\mathbf{x}, \omega) = \left(\frac{\omega x_3 c}{4\pi c_0 S_0^2} \right)^2 2\pi d \sum_{m=-\infty}^{\infty} \left| \mathcal{L}(\omega, \bar{k}_1, 2m\pi/\lambda) \right|^2 \Pi(\omega, 2m\pi/\lambda). \tag{2.55}$$

Equation (2.55) is the fundamental result of this paper and it is interesting to note that the infinite series in (2.55) appears similar to that in Howe's model shown in (4.2). For example, both results show that the PSD of far-field sound is related to the wavenumber spectral density of the surface pressure through $\Pi(\omega, 2m\pi/\lambda)$, therefore a skewed wall pressure gust with $k_2 = 2m\pi/\lambda$ plays an important role in sound generation.

2.4. *Discussion on the effects of serration geometry*

The complicated formulation of the far-field noise (2.55), and the response function (2.43), make it very difficult to assess the effectiveness of serrations without numerical evaluation of the equations. This section attempts to derive two simple conditions for serrations to obtain effective noise reduction. In order to achieve significant sound reduction, we wish to minimize (2.55). Since $|\mathcal{L}(\omega, \bar{k}_1, 2m\pi/\lambda)|^2$ is very complex, we will perform an order analysis first.

Careful examination of (2.43) shows that $|\mathcal{L}|^2$ is proportional to $1/|\kappa_{n'j}|^2$. For illustration purposes, we assume that the observer is at $90°$ above the trailing-edge in the mid-span plane, i.e. $x_1 = 0$ and $x_2 = 0$, and that the Mach number is low, e.g. $M_0 < 0.2$. Then $\kappa_{mj} \approx 0$ when m satisfies $k_2 + 2m\pi/\lambda \approx 0$ and thus the value of $|\mathcal{L}(\omega, \bar{k}_1, -2m\pi/\lambda)|^2$ is dominated by mode m, i.e.

$$|\mathcal{L}(\omega, \bar{k}_1, -2m\pi/\lambda)|^2 \approx \frac{2}{\lambda^2 c^2} \left| a_m Q_{mm} + \Theta_m^{(1)} + \Theta_m^{(2)} + \cdots \right|^2. \tag{2.56}$$

Furthermore, noting that $v_{nm} = 4h/(\pi^2(n-m)^2)$ when $n-m$ is odd, equation (2.44)

suggests that $\Theta_m^{(i)}$ may roughly be approximated by only summing over modes $m-1$ and $m+1$, since higher orders $m \pm (2j+1)$ with $j \geqslant 1$ are at least one order of magnitude smaller due to the quadratic term in the denominator of v_{nm}. Using this approximation, $\Theta_m^{(i)}$ varies linearly with a_{m-1} and a_{m+1}. From the definition of a_m in (2.20), it can be shown that

$$a_m = \frac{e^{im\pi/2}}{2}\mathrm{sinc}(k_1 h - m\pi/2) + \frac{e^{-im\pi/2}}{2}\mathrm{sinc}(k_1 h + m\pi/2). \tag{2.57}$$

Therefore, $|a_{m-1}|$ and $|a_{m+1}|$ are of the order of $|a_m|$ and $|\Theta_m^{(i)}| = O(|a_m|)$. From (2.56), we hence have $|\mathcal{L}(\omega, \bar{k}_1, -2m\pi/\lambda)|^2 = O(|a_m|^2)$, and

$$\sum_{m=-\infty}^{\infty} |\mathcal{L}(\omega, \bar{k}_1, 2m\pi/\lambda)|^2 \Pi(\omega, 2m\pi/\lambda) = O\left(\sum_{m=-\infty}^{\infty} |a_m|^2 \Pi(\omega, 2m\pi/\lambda)\right). \tag{2.58}$$

We are now in a position to discuss the conditions for minimizing (2.58). It is clear from (2.57) that $|a_m|$ is maximum when $m \approx \pm\nu_0$, where $\nu_0 = 2k_1 h/\pi$. To minimize the right hand side in (2.58), we therefore require that $\Pi(\omega, 2m\pi/\lambda) \ll \Pi(\omega, 0)$ when m approaches $\pm\nu_0$. Assuming frozen turbulence, $\Pi(\omega, 2m\pi/\lambda)$ is given by

$$\Pi\left(\omega, \frac{2\pi m}{\lambda}\right) = \frac{1}{2\pi} \int_{-\infty}^{\infty} S_{qq}(\omega, y') e^{-i\frac{2\pi m}{\lambda}y'} \, dy'. \tag{2.59}$$

When $2\pi\nu_0 l_{y'}/\lambda = k_1 l_{y'}\sigma \gg 1$, the integrand in (2.59) for m close to (or larger than) ν_0 oscillates rapidly within the length scale $l_{y'}$ of $S_{qq}(\omega, y')$, which corresponds to the spanwise correlation length given by

$$l_{y'}(\omega) = \frac{1}{S_{qq}(\omega, 0)} \int_{-\infty}^{\infty} S_{qq}(\omega, y') \, dy'. \tag{2.60}$$

The integral in (2.59) therefore evaluates to a small value compared to $\Pi(\omega, 0)$. Thus, a condition for noise reduction is that $k_1 h_e \gg 1$, where we have defined an effective root-to-tip amplitude $2h_e = \sigma l_{y'}$ that describes the correlated serration amplitude.

As $2k_1 h_e = k_1 \sigma l_{y'}(\omega)$, the decay rate of spanwise correlation length $l_{y'}(\omega)$ with respect to frequency is critical. If one makes use of Corcos's correlation length model (Corcos 1964), $l_{y'}(\omega) \approx 2.1U_c/\omega$, $k_1 h_e$ will reduce to a constant, in this case 2.1σ, a sole function of the serration sharpness factor and independent of frequency. This is consistent with the findings of Howe (1991*b*). However, if the decay rate were faster than that given by Corcos, no sound reduction or even some sound increase would occur at high frequencies. An accurate description of the characteristics of the surface pressure fluctuation beneath a boundary layer is therefore critical for the model to accurately predict the sound reduction at high frequencies.

Note that the condition $k_1 h_e \gg 1$ is only a necessary condition, because when $k_1 h \to 0$ there is no noise reduction. This can be seen from equation (2.58), since $a_m = 0$ when $k_1 h \to 0$ except when $m = 0$, so the right hand side in equation (2.58) reduces to $\Pi(\omega, 0)$ which corresponds to the straight edge case. From (2.57), for a given integer m away from ν_0, $|a_m|$ tends to zero when $k_1 h \gg 1$. This provides another necessary condition for noise reduction. Physically, the root-to-tip amplitude of the serrations must be sufficient for them to be seen by the incoming hydrodynamic waves.

We have thus obtained two necessary conditions for noise reduction, $k_1 h_e \gg 1$ and $k_1 h \gg 1$, that are consistent with those proposed by Howe. These conditions will be further investigated in Sec. 5.

3. Results

3.1. *Model Validation*

3.1.1. *FEM implementation*

For the coupled differential equations mentioned in the last section, the solutions are obtained by performing an iterative-solving procedure. In this section, we shall investigate the validity of the proposed iterative solution using the Finite Element Method (FEM). Instead of solving the far-field sound directly, costing a significant amount of computer memory, a feasible alternative is to calculate the near field using FEM and obtain the far-field solution by performing a surface integral, as adopted in analytical models, see (2.40).

In order to make a direct comparison between the computational and analytical results, the wave equation together with the boundary conditions given in (2.5) and (2.4), respectively, will be solved. The governing equation and boundary conditions in the frequency domain can be written as,

$$
\begin{cases}
\beta^2 \dfrac{\partial^2 P}{\partial x'^2} + \dfrac{\partial^2 P}{\partial y'^2} + \dfrac{\partial^2 P}{\partial z'^2} + 2ikM_0 \dfrac{\partial P}{\partial x'} + k^2 P = 0, & \\
\dfrac{\partial P}{\partial z'}(x', y', 0) = 0, & x' < H(y') \\
P(x', y', 0) = -P_i e^{i(k_1 x' + k_2 y')}, & x' \geqslant H(y').
\end{cases} \tag{3.1}
$$

Using the transformation $P = \bar{P}e^{-ikM_0 x'/\beta^2}$, the first-order derivative term, induced by the background flow, can be eliminated. The results will be transformed back to the physical domain before making comparisons. The scattered near-field pressure is obtained by solving (3.1) using FEM and the far-field sound pressure is obtained by integrating the pressure distribution over surface, as described in (2.40) and (2.41).

The commercial software COMSOL 4.4 is used to perform the FEM simulations. Simulations are performed for a single serration, as shown in figure 3. The domain size is approximately L in the streamwise and $L/2$ in the vertical direction. The length L depends on the frequency while chord length c over which the surface integral is performed is kept constant. To eliminate the effect of leading-edge back-scattering and have a fast convergence, L is taken to be at least twice the sound wavelength. For the boundary conditions, the normal velocity on the surface of the plate vanishes, while the pressure values are fixed over the wake half plane (the surface denoted by "Wake") in figure 3. To eliminate the scattering effect of the edge between the "Wake" and its adjacent PML surfaces, a Gaussian weighted pressure is given, as can be seen on the "Wake" surface in figure 4. In addition, as illustrated in figure 3, the walls on both the upper and lower sides of computational domain represent Floquet periodic boundary conditions. The radiation boundary condition is implemented via Perfectly Matched Layers (PMLs), as shown in figure 3. The mesh is made of tetrahedron cells with quadratic shape functions. The mesh is highly non-uniform and is generated to accurately resolve the hydrodynamic pressure fluctuations near the serrated edge and the acoustic pressure perturbation in the far-field. A mesh sensitivity test has been carried out to ensure the proper convergence of the simulation. In the hydrodynamic region, the mesh contains more than 10 grid points within one hydrodynamic wavelength. The ratio of 16 grid points per wavelength is used in the far-field, relative to the acoustic wavelength. The finest mesh for the highest frequency contains about 3.0 million elements. Note that at low frequencies (e.g. $kc \approx 1$) the computational domain has a very large aspect ratio, which might cause larger numerical errors.

Figure 4 shows the results for a straight trailing-edge at $kc \approx 18$ and $M = 0.1$.
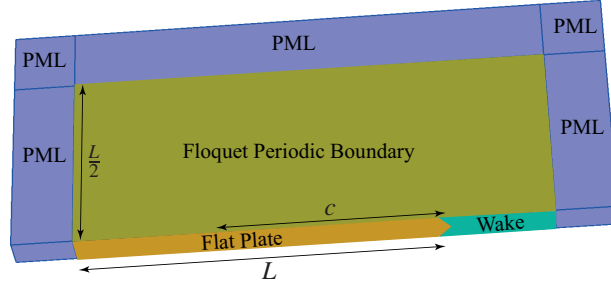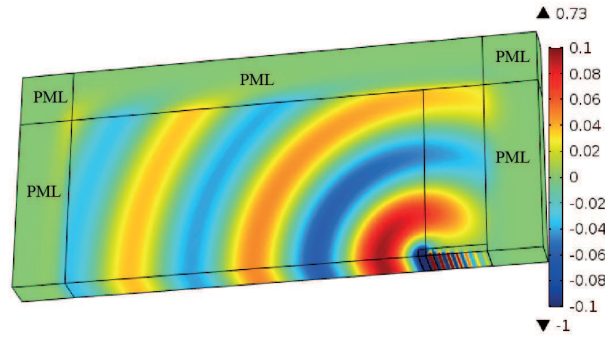
FIGURE 3. Illustration of the FEM computing domain and the boundary conditions.

FIGURE 4. The computed pressure distribution scattered by a straight trailing-edge at $kc = 18$ and $M_0 = 0.1$.

The turbulent convection velocity is assumed to be $U_c = 0.7U$, where $U = M_0 c_0$. The wavenumbers are $k_1 = 2\pi f/U_c$, $k_2 = 0$ and the amplitude of incident wall pressure gust P_i is unity. It can be seen that the PMLs do not cause spurious reflections. As the straight-edge scattering is a 2D problem which is implemented in a 3D domain to perform FEM sensitivity analysis, a sweep mesh is used to avoid the high-aspect-ratio problems at low frequencies. The solution was also compared with Amiet's analytical solution. The maximum difference at all frequencies ($1 < kc < 40$) was less than 1%.

3.1.2. *FEM model validation*

This section provides a comprehensive comparison between the analytical model for gust-induced far-field noise developed in Sec. 2.3.2 and the FEM model developed in Sec. 3.1.1 for different serrations and at different Mach numbers. The far-field sound pressure induced by a wall pressure gust of $k_2 = 0$ at different frequencies is chosen for comparison. Note that in the mathematical model, we use the second-order approximation of the gust-response function $\mathcal{L}$, as shown in (2.43). The span-to-chord ratio is chosen to be 8. The Mach number and geometrical shape of the serrations can vary in different cases.

Results are presented for a range of serrations, as illustrated in figure 5(a) through 5(f). In this study, we shall only focus on low Mach numbers, i.e. $M_0 \leqslant 0.2$. The far-field pressure, obtained from the FEM model at 90° above the trailing-edge in the mid-span plane with $x_3/c = 1$, is plotted as $20\log_{10}|p_f(\mathbf{x}, \omega)|$ against the theoretical predictions. Results are provided for both the straight(no serration, i.e. $h = 0$) and serrated trailing-edges. It can be found that a sound reduction of more than 20 dB can be achieved for
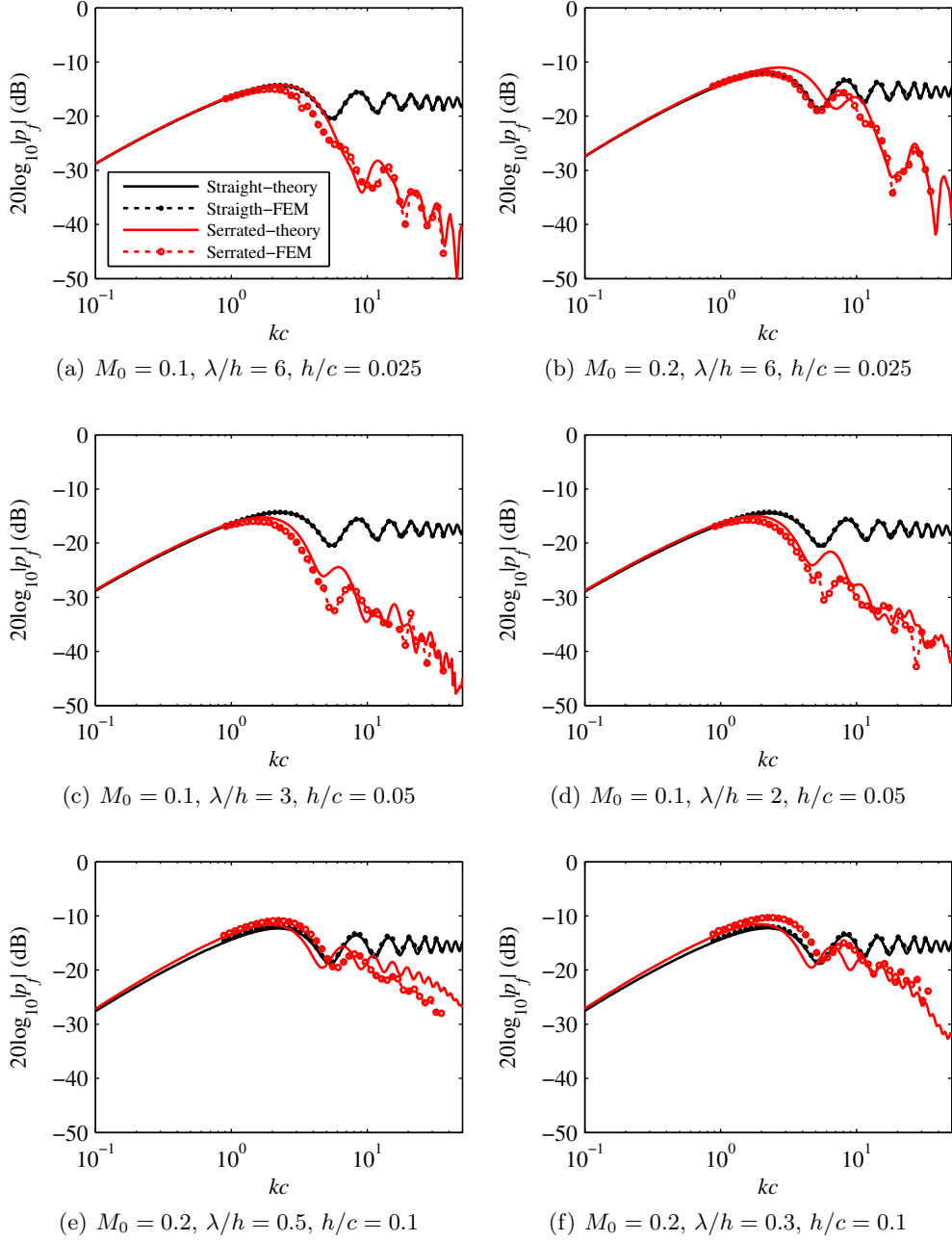
FIGURE 5. Trailing-edge noise Sound Pressure Level (SPL) in the mid-span plane at $\theta = 90°$ and $x_3/c = 1$ above the plate, due to a wall pressure gust with $k_2 = 0$.

the far-field sound induced by this specific wall pressure gust. This reduction should however not to be confused with the sound reduction of the real trailing-edge noise, which comprises different wall pressure gusts at different values of k_2.

Figures 5(a) to 5(d) show good agreement between the theoretical and computational results. In particular excellent agreement is achieved for straight edge cases at all fre-

quencies because its 2D simplicity. The low frequency discrepancies for serrated cases, however, might be due to the error caused by the aforementioned high-aspect-ratio problems.The serration cases presented in figures 5(a) to 5(d) are not normally considered sharp enough, based on experimental observations (Gruber 2012) to reduce the noise significantly. Figures 5(e) and 5(f) show the results at $M_0 = 0.2$ for serrations with $\lambda/h = 0.5$ and $h/c = 0.1$ and $\lambda/h = 0.3$ and $h/c = 0.1$, respectively. It can be seen from these two figures that for sharper serrations, the average error between the numerical calculations and theoretical predictions normally increases, which might be caused by the relatively slower convergence rate of the second-order approximations of (2.43) compared to that for the wide serrations. The agreement between the FEM results and the proposed model, however, is generally good, suggesting that the second-order solution does indeed give a reasonable good approximation for (2.43). The issue of the convergence of the iterative method will also be discussed later.

3.2. *The far-field sound spectrum*

A parametric study of far-field noise reduction was carried out by Howe (Howe 1991b,a), indicating the possibility of significant noise reduction, much higher than measured data (Gruber 2012). In this section, we shall use the second-order iterative model developed in Sec. 2 and carry out a parametric study. For illustration purposes, we adopt Chase's model (Chase 1987) of the wavenumber spectral density. It is argued by Chase (1987) that the convection velocity U_c is weakly dependent on frequency and on average $U_c \approx 0.7U$. According to Chase's model, the wavenumber spectral density is well approximated by

$$\Pi(\omega, k_1, k_2) = \frac{C_m \rho_0^2 v_*^3 k_1^2 \delta^5}{((k_1 - \omega/U_c)^2 (\delta U_c v_*/3)^2 + (k_1^2 + k_2^2)\delta^2 + \chi^2)^{5/2}}, \tag{3.2}$$

where ρ_0 is the density of air, and $C_m \approx 0.1553, \chi \approx 1.33, v_* \approx 0.03U$. The turbulent boundary layer thickness δ in (3.2) is approximated by (Eckert & Drake 1959)

$$\delta/c = 0.382 Re_c^{-1/5}, \tag{3.3}$$

here Re_c is the Reynolds number based on chord c. An inspection of (3.2) shows that the wavenumber spectrum peaks around $k_1 = \omega/U_c$. Here, we make use of the fact and obtain $\Pi(\omega, k_2)$ by integrating (3.2) with respect to k_1 and then keeping the leading order terms (Howe 1991b), which yields

$$\Pi(\omega, k_2) \approx \frac{4C_m \rho_0^2 v_*^4 (\omega/U_c)^2 \delta^4}{U_c \left(((\omega/U_c)^2 + k_2^2)\delta^2 + \chi^2\right)^2}. \tag{3.4}$$

Substituting (3.4) into (2.55) and using $(\rho_0 v_*^2)^2 (d/c_0)$ (Howe 1991b) to non-dimensionalize the far field PSD yields

$$\frac{S_{pp}(\mathbf{x}, \omega)}{(\rho_0 v_*^2)^2 (d/c_0)} = \frac{C_m}{2\pi} \Psi(\mathbf{x}, \omega), \tag{3.5}$$

where $\Psi(\mathbf{x}, \omega)$ is defined as

$$\Psi(\mathbf{x}, \omega) = \left(\frac{x_3 c}{S_0^2}\right)^2 \left(\frac{U_c}{c_0}\right) \sum_{m=-\infty}^{\infty} \left|\mathcal{L}(\omega, \bar{k}_1, 2\pi m/\lambda)\right|^2 \frac{(\omega\delta/U_c)^4}{[(\omega\delta/U_c)^2 + (2m\pi\delta/\lambda)^2 + \chi^2]^2}. \tag{3.6}$$

The following figures are plotted using (3.6) for a variety of serration geometrical parameters. Since much of the experimental work focused on the trailing-edge noise at low
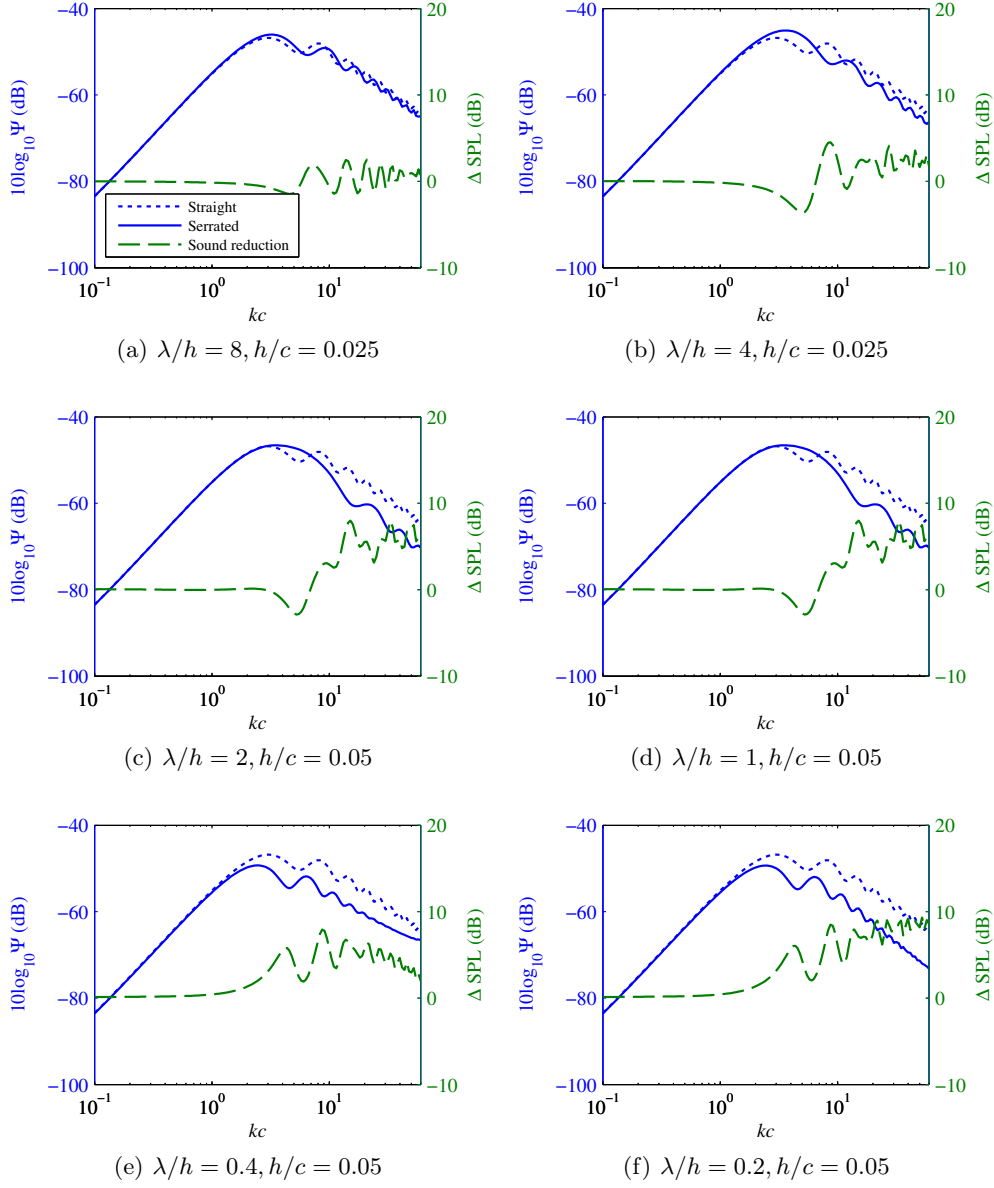
FIGURE 6. The normalized spectrum of equation (3.6) (left axis) for serrated and straight trailing-edges (in solid and dotted blue lines respectively) and the sound reduction spectrum ΔSPL (right axis and in green dashed line) for an observer at $\theta = 90°$ and $x_3/c = 1$ above the plate in the mid-span plane with $M_0 = 0.1$.

Mach numbers (Gruber *et al.* 2013), we shall only focus on the low Mach numbers, i.e. $M_0 \leqslant 0.2$. The function $\mathcal{L}$ in (3.6) is defined in (2.43) and we take the second-order approximation here. Note that the incident pressure is also taken into consideration (Amiet 1978). The observer point is at $90°$ above the trailing-edge in the mid-span plane, namely $(x_1/c = 0,\ x_2/c = 0,\ x_3/c = 1)$. It is worth pointing out that in figure 6 both the far-field sound spectrum and the sound reduction spectrum are shown.
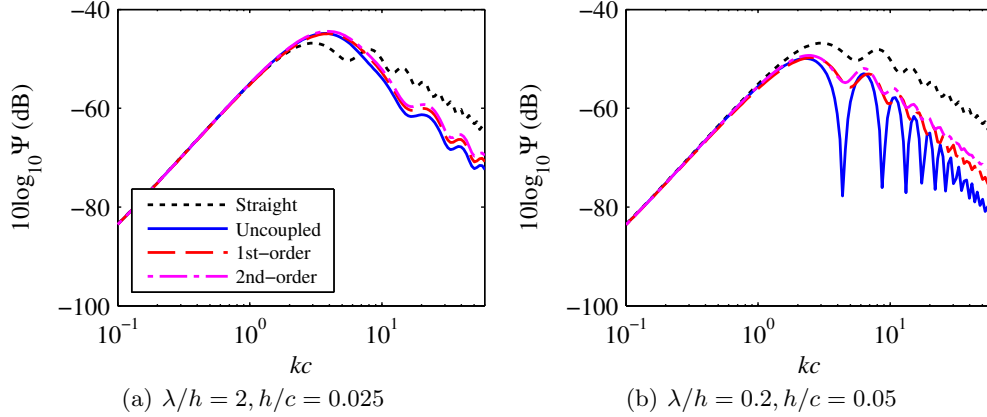
FIGURE 7. The normalized spectrum for straight and serrated trailing-edges obtained using different order approximations, for an observer at $\theta = 90°$ and $x_3/c = 1$ above the plate in the mid-span plane with $M_0 = 0.1$.

The normalized sound power spectrum at $M_0 = 0.1$ for different serrations are shown in figures 6(a) to 6(f). The spectrum for a serrated trailing-edge with $4h/\lambda = 0.5$ is shown in figure 6(a). As expected, the sound reduction is approximately zero over the entire the frequency range of interest. Increasing the sharpness of the serrations gradually improves the sound reduction performance, as shown in figures 6(b), 6(c) and 6(d). For sufficiently sharp serrations, significant sound reduction is achieved over a wide range of frequencies, as shown in figure 6(e), where the sharpness factor is $4h/\lambda = 10$. The result obtained for a sawtooth serration with $\lambda/h = 0.2, h/c = 0.05$ at $M_0 = 0.1$ is shown in figure 6(f). Comparing figures 6(e) and 6(f) suggests that for already sharp serrations, further increasing the sharpness can provide a better high frequency noise reduction performance while the low frequency performance ($kc < 10$) remains unchanged. For the sharp serrations presented in figure 6(f) the far-field sound is reduced by about 10 dB at high frequencies. This better agrees with experiments where a noise reduction of up to $7-10$ dB is observed (Dassen *et al.* 1996; Parchen *et al.* 1999). From figure 6(a) and 6(b) it can be found that a slight noise increase may occur at low frequencies. In fact, the noise increase becomes even more pronounced at low frequencies when the Mach number is high, e.g. $M_0 = 0.4$. The explanation of the noise increase at low frequencies will be given in Sec. 5.

The results presented in figure 6 were based on the second-order approximation. The convergence rate of different order solutions can be inspected by presenting the far-field sound spectrum using different-order approximations, as shown in figure 7, where the far-field spectrum using zero, first and second-order approximations are presented. Figure 7(a) presents results for a wide serration with $\lambda/h = 2$. As expected, due to the weak coupling between different modes the first and second-order solutions yield almost the same results. It is thus safe to assume that the second-order approximation gives an accurate solution for wide serrations. Figure 7(b) shows the convergence results for a narrow serrations with $\lambda/h = 0.2$. It can be seen that the difference between the first and second-order solutions is much smaller than that between the zero- and first-order ones. The maximum difference between the first and second-order approximations at high frequencies is less than 2 decibels. Thus, the second-order solution can be assumed to provide a reasonably accurate solution for narrow serrations even at high frequencies.

3.3. *Directivity patterns*

It is a well established fact that the trailing-edge noise directivity changes with frequency (Williams & Hall 1970; Gruber *et al.* 2013). However, the effect of serrations on trailing-edge noise directivity has received very little research attention. Figures 8 and 9 present the non-dimensional far-field PSD, (3.6), based on the second-order solution. Results are presented for straight and serrated trailing-edges with $\lambda/h = 0.4$ at $M_0 = 0.1$ and 0.4, respectively. As expected, using serrations has little effect on noise generation mechanism at very low frequencies, $kc \leqslant 1$. Results, however, show that the serrations can effectively reduce the noise at higher frequencies. As discussed earlier, this is believed to be primarily due to the destructive scattering interference effects. While most experimental investigations (Gruber *et al.* 2013) have focused on the capability of serrations for reducing the noise at small angles and 90 degrees above the trailing-edge, results in figures 8 and 9 clearly show that serrations are more effective in reducing the noise at large radiation angles, i.e. towards the leading-edge, $\theta > 90°$. This is a very interesting result as noise measurement in laboratory environment is often limited to 30 to 120 degrees due to the anechoic chamber room size constraint or reflection by the contraction nozzle, etc (Gruber 2012; Moreau & Doolan 2013).

Results have also shown that the use of serrations can lead to significant changes to the directivity pattern of the scattered pressure field at high frequencies. While one would expect a cardioid pattern for straight edges at high frequencies, associated with the edge scattering of a half-plane (Williams & Hall 1970), results for serrated trailing-edges show that the directivity pattern is more dipolar with a clear peak at a specific angle which depends on both the serration sharpness and the Mach number. Numerical study of the directivity pattern for different serrations has shown that the expected cardioid shape gradually changes to a more dipolar shape as the serration sharpness increases and the directivity peak also gradually moves downstream, towards the trailing-edge. The dipolar behaviour of the noise from serrated trailing-edges means that the leading-edge region, $\theta = 180°$, is much quieter than that for straight trailing-edge. Increasing the Mach number also appears to move the peak angle towards the trailing-edge, as can be seen by comparing figures 8 and 9. It is also worth mentioning that in the case of high Mach numbers, see figure 9, the use of serrations can lead to considerable noise increase in the trailing-edge region ($0° < \theta < 90°$), for intermediate frequencies, $1 < kc < 10$.

4. Comparison with Howe's model

The mathematical model and serration geometrical criteria developed by Howe have long been used as a tool to evaluate the effectiveness of trailing-edge serrations and estimate the level of noise reduction (Gruber 2012; Azarpeyvand *et al.* 2013; Jones & Sandberg 2012). However, it has repeatedly been shown that Howe's model overpredicts the level of noise reduction (Dassen *et al.* 1996; Parchen *et al.* 1999; Gruber 2012). To simplify the model, Howe assumes that the Mach number is sufficiently low to neglect the convection effect, the frequency are sufficiently high, satisfying $\omega h/U_c \gg 1$, the statistical property of the turbulence inside the boundary layer remains the same before and after passing the trailing-edge and the diffraction model is based on the Green's function for straight trailing-edges and the slender-wing approximations.

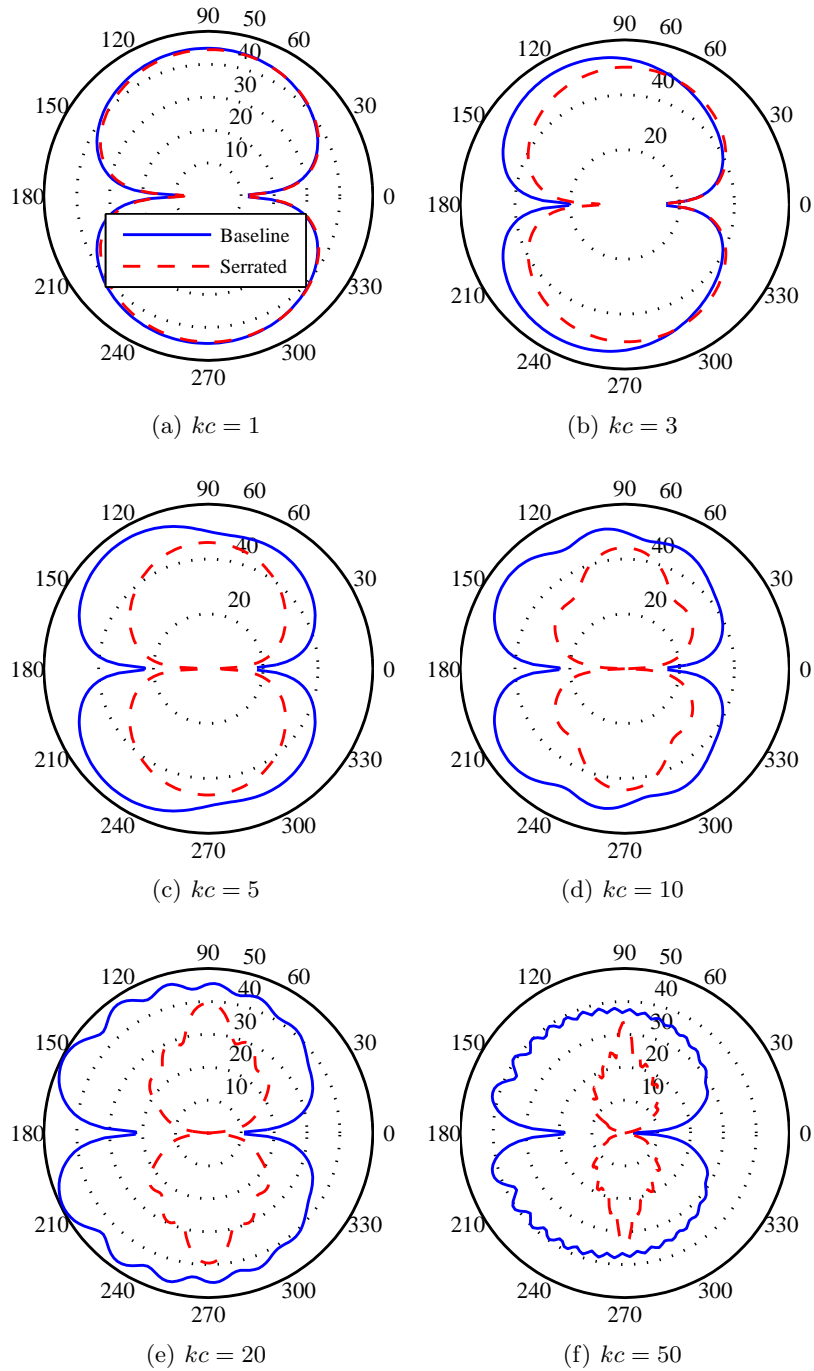With the introduction of Chase's surface pressure wavenumber spectral density Model,

FIGURE 8. The directivity patterns plotted against θ in the mid-span plane ($x_2 = 0$ and $\sqrt{x_1^2 + x_3^2}/c = 1$) at $M_0 = 0.1$ for serrations with $\lambda/h = 0.4$ and $h/c = 0.05$. The far-field sound level in the figures are $10\log_{10}\left(\Psi(\mathbf{x}, \omega)/(4 \cdot 10^{-10})\right)$.
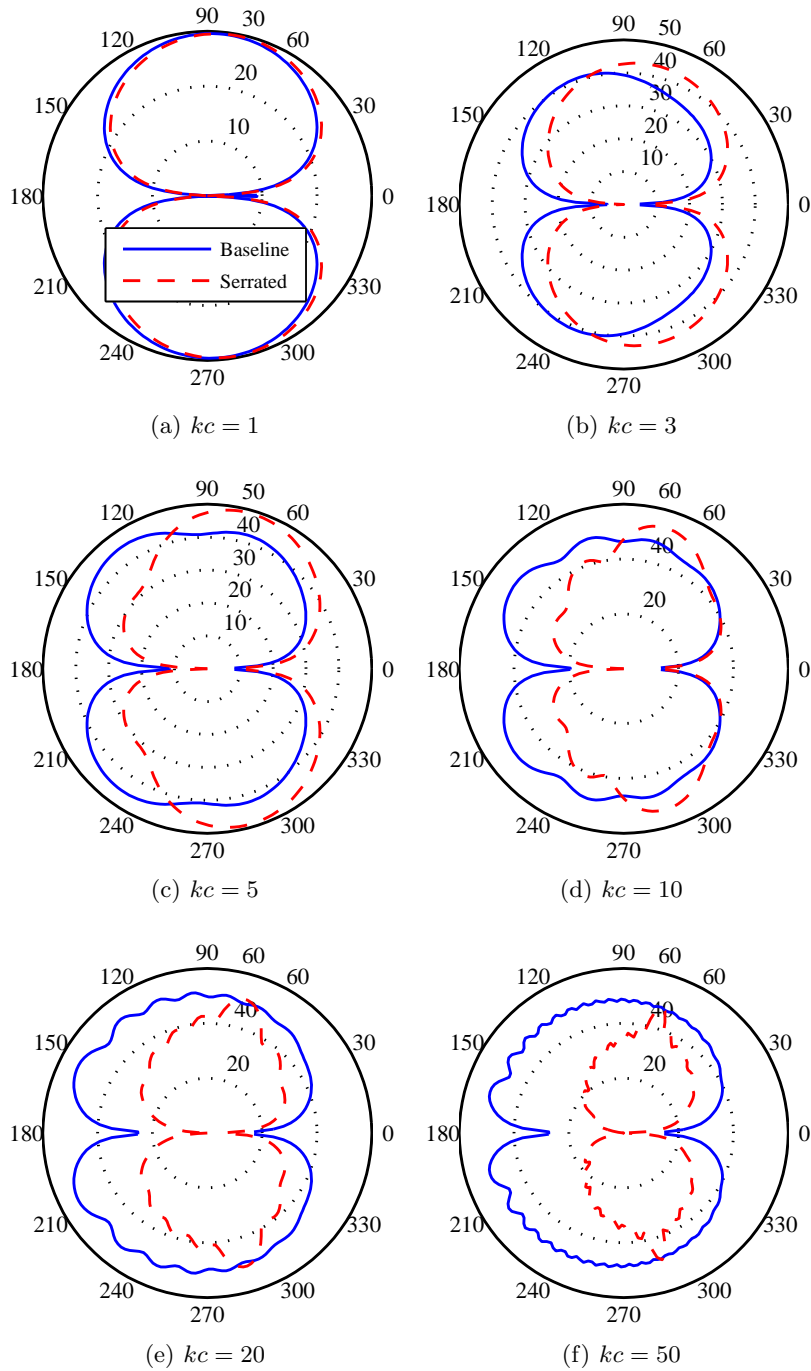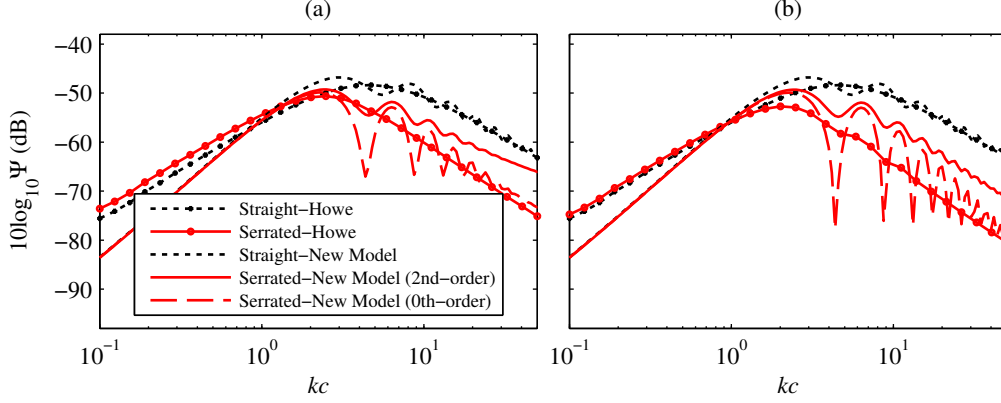
FIGURE 9. The directivity patterns plotted against θ in the mid-span plane ($x_2 = 0$ and $\sqrt{x_1^2 + x_3^2}/c = 1$) at $M_0 = 0.4$ for serrations with $\lambda/h = 0.4$ and $h/c = 0.05$. The far-field sound level in the figures are $10\log_{10}\left(\Psi(\mathbf{x},\omega)/(4\cdot 10^{-10})\right)$.

FIGURE 10. The normalized spectrum of Howe's model and the new model, the observer is at $90°$ above the trailing-edge in the mid-span plane with $x_3/c = 1$. (a): $\lambda/h = 0.4$, $h/c = 0.05$, $M_0 = 0.1$; (b): $\lambda/h = 0.2$, $h/c = 0.05$, $M_0 = 0.1$.

Howe (Howe 1991a) shows that the far-field PSD is given by

$$\frac{S_{pp}(\omega, \mathbf{x})}{(\rho_0 v_*^2)^2 (d/c_0)(\delta/|\mathbf{x}|)^2} = \frac{C_m}{\pi} \sin^2(\theta/2) \sin(\phi) \Psi_f(\omega), \tag{4.1}$$

where

$$\Psi_f(\omega) = 8(h/\delta)^2 \sum_{m=-\infty}^{\infty} \frac{(\omega h/U_c)^2[(\omega h/U_c)^2 + (2m\pi h/\lambda)^2][1 - \cos(2\omega h/U_c)/\cos(m\pi)]}{[(2\omega h/U_c)^2 - m^2\pi^2]^2[(\omega h/U_c)^2 + (2m\pi h/\lambda)^2 + (\chi h/\delta)^2]^2}. \tag{4.2}$$

Even though the assumption of frozen turbulence is used in both models, Howe's model differs from the model presented in this paper in several ways. In Howe's model, the far-field sound pressure is based on a compact Green's function. The Green's function is obtained by making use of the slender wing approximation. The model developed in this paper, however, gives the scattered sound by solving the convected wave equation. Howe's model neglects the effects of convection, so it is only valid at low Mach numbers. The new model is valid for any subsonic Mach number, as the convection effects have been incorporated in the convected wave equation. In addition, Howe's model requires the high frequency condition $\omega h/U \gg 1$, while the new model requires $kc > 1$, as an semi-infinite chord is assumed in the derivation.

Figures in this section represent the results obtained using Howe's model, i.e. (4.1), and the model developed in this paper, i.e. (3.5). The normalized spectrum $\Psi(\mathbf{x}, \omega)$ is defined in the same way as in (3.5). The result of the new model with the correction applied to the third term in (2.46), according to Amiet (1978), systematically increases the noise level by 6 dB. Figure 10(a) shows the noise prediction results for a serrated trailing-edge with $\lambda/h = 0.4, h/c = 0.05$ at $M_0 = 0.1$ using both models. The comparison of the results shows a clear difference between the two methods. At high frequencies, e.g. $kc \approx 50$, Howe's model gives a sound reduction of about 13 dB while the new model predicts about 7 dB of noise reduction. Figure 10(b) presents the comparison for sharper serrations, with $\lambda/h = 0.2, h/c = 0.05$ at $M_0 = 0.1$. At $kc \approx 50$, the noise reduction predicted by Howe's model and the new model are, respectively, 18 dB and 10 dB. It can be interpreted from the results that the new model provides a much more realistic noise

reduction estimate and is more consistent with experimental observations (Dassen *et al.* 1996; Parchen *et al.* 1999; Gruber 2012; Gruber *et al.* 2013).

It is very interesting to note that the zero-order solution accurately follows Howe's solution at high frequencies, as shown in figure 10. At intermediate frequencies, i.e. $2 < kc < 20$, the zero-order solution oscillates strongly, but the mean value seems to be following Howe's result. This is actually not hard to understand, as the Green's function used in Howe's model (Howe 1991*a*), is in fact only valid locally. In other words, it does not include the coupling effect between adjacent sawtooth edges. Thus, at high frequency we expect the zero-order (without the coupling effect induced by the singular root and tip points) solution coincides with Howe's results. The high-order solution, however adds the coupled interactions between different modes, and this coupling effect clearly reduces the sound reduction predicted by the zero-order solution at high frequencies. Thus, the large overprediction of Howe's model is likely to have been caused by the choice of the Green's function since the Green's function is not able to take into account the coupling effects.

5. Noise reduction mechanism

In order to better understand the noise reduction mechanism, the pressure distribution over the flat plate surface is presented, see figures 11 to 14. As mentioned earlier, the incident pressure only raises the far-field sound by 6 dB systematically, thus it suffices to consider the scattered pressure distribution only. The scattered pressure, as mentioned in Sec. 2, is essentially the pressure jump across the flat plate. As mentioned in Sec. 2.4, the two non-dimensional parameters $k_1 h$ and $k_1 h_e$ play an important role for effective sound reduction using serrated trailing-edges. In what follows, the scattered pressure distribution will be presented by fixing one parameter and varying the other. Note that the scattered pressure mentioned here is due to wall pressure gusts with $k_2 = 0$. The discussion, however, also applies to gusts with $k_2 \neq 0$, as the streamwise number k_1 has the same value for different gusts.

The scattered pressure on the flat plate is presented in figure 11 for different values of $k_1 h$. The scattered surface pressure is obtained by evaluating the real part of (2.39) using the second-order approximation ($P_i = 1$) and then normalizing to unity. The results presented in figure 11 are obtained for $k_1 h_e = 7$, while $k_1 h$ varies between 2 and 20. The spanwise coordinate y' is normalized by the spanwise correlation length $l_{y'}$ and the streamwise coordinate x' is normalized by the hydrodynamic wavelength $\lambda_1 = 2\pi/k_1$. Thus, the distance between the two adjacent streamwise dashed lines corresponds to the spanwise correlation length, $l_{y'}$. Figure 11(a) plots the scattered surface pressure distribution near the trailing-edge for $k_1 h = 2$. It shows that the scattered surface pressure field between two adjacent streamwise lines is essentially in phase, so no strong phase variation within $l_{y'}$ occurs. Figure 11(b) shows the scattered surface pressure distribution for $k_1 h = 4$, and it can seen that little phase differences appear within a spanwise correlation length. Figure 11(c) shows the scattered surface pressure distribution for $k_1 h = 10$. It is clear that even if the spanwise correlation length becomes smaller, a pronounced phase difference still appears within adjacent streamwise lines. Further increasing the value of $k_1 h$ to 20, as shown in figure 11(d), decreases the spanwise correlation length, but enough phase difference still appears within the increasingly narrow ranges.

To make the phase variation induced by the presence of serrations even clearer, the scattered surface pressure along the trailing-edge is presented in figure 12. Each line corresponds to a different value of $k_1 h$. The real and imaginary parts of the pressure are shown in figure 12(a) and 12(b), respectively. The two figures are thus showing the pres-
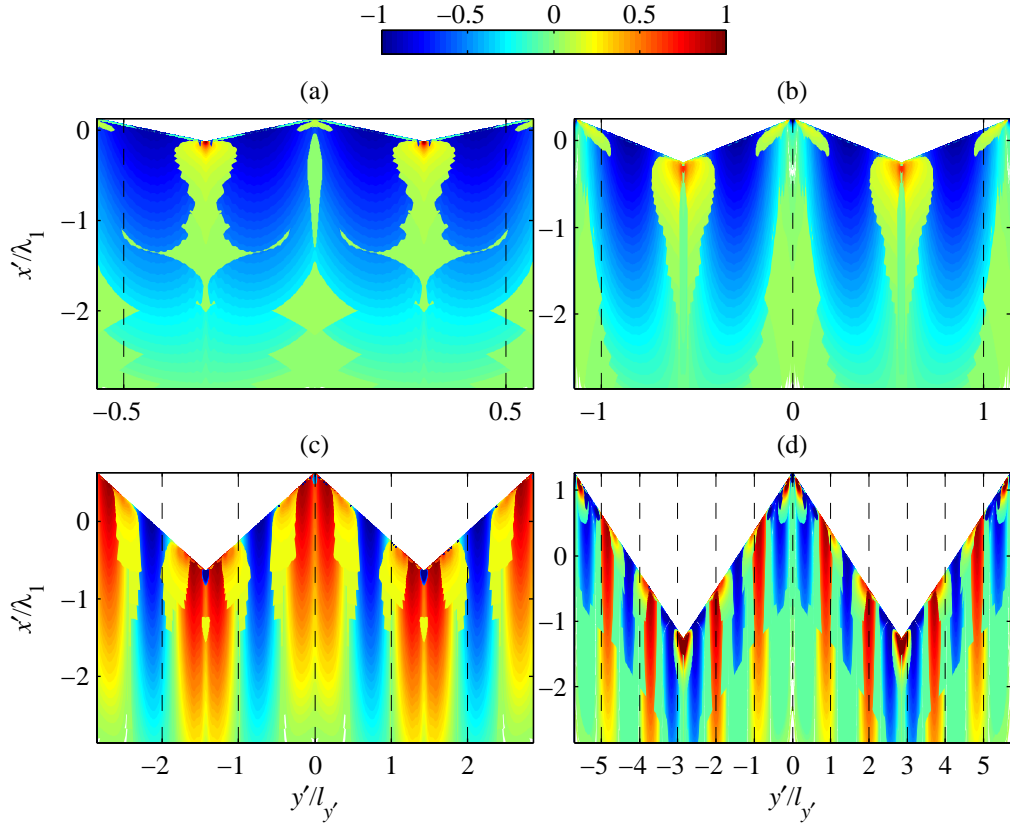
FIGURE 11. The scattered surface pressure distribution at a fixed frequency for the same $k_1 h_e = 7$. (a): $k_1 h = 2$; (b): $k_1 h = 4$; (c): $k_1 h = 10$; (d): $k_1 h = 20$. The horizontal axis shows the spanwise coordinate normalized by the spanwise correlation length and the vertical axis shows the streamwise coordinate normalized by the hydrodynamic wavelength.
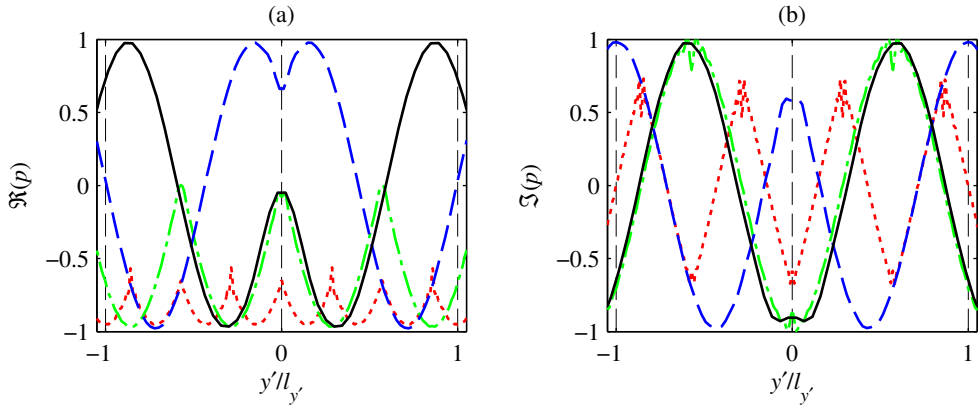

FIGURE 12. Scattered pressure on the serrated edge with red dotted line for $k_1 h = 2$, green dot-dashed line for $k_1 h = 4$, blue dashed line for $k_1 h = 10$ and black solid line for $k_1 h = 20$. (a): real part; (b): imaginary part.
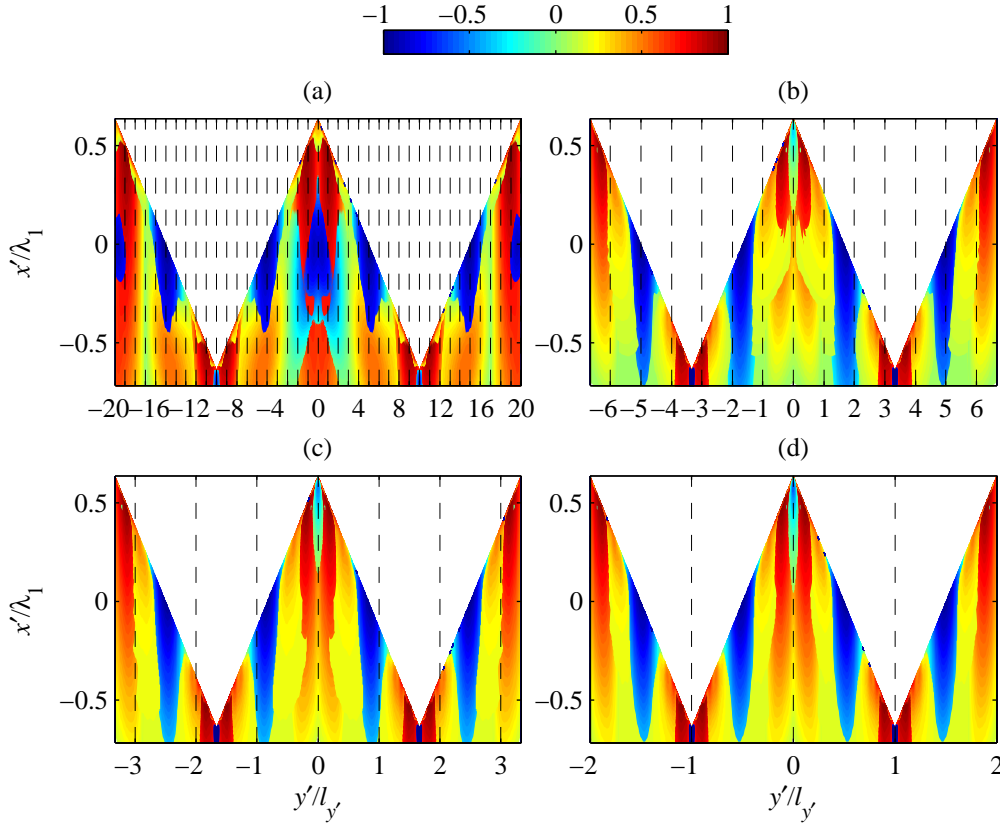
FIGURE 13. The scattered surface pressure distribution for different serrations at a fixed frequency and $k_1 h = 10$. (a): $k_1 h_e = 1$; (b): $k_1 h_e = 3$; (c): $k_1 h_e = 6$; (d): $k_1 h_e = 10$. The horizontal axis shows the spanwise coordinate normalized by the spanwise correlation length and the vertical axis shows the streamwise coordinate normalized by the hydrodynamic wavelength.

sure distributions at different instants. The red curve in figure 12(a), which corresponds to the real part for $k_1 h = 2$, remains almost entirely negative. The corresponding imaginary part, shown in red in figure 12(b), has a phase which slightly changes signs over $l_{y'}$. Since the signal oscillates between the real and imaginary parts, the phase changes sign only over a small fraction of the cycle. The black curves corresponding to $k_1 h = 20$, on the other hand, show a strong variation within a spanwise correlation length in both figure 12(a) and 12(b), indicating a strong phase variation over the whole cycle. Therefore, the phase differences of the scattered pressure are more likely to be strong and permanent for high values of $k_1 h$.

The scattered pressure distributions for different values of $k_1 h_e$ are presented in figure 13. The values of $k_1 h$ is fixed at 10 while $k_1 h_e$ increases from 1 to 10 (see figures 13(a) to 13(d)). The spanwise and streamwise coordinates are also normalized by $l_{y'}$ and λ_1, respectively. Figure 13(a) presents the scattered surface pressure distribution for $k_1 h_e = 1$. As $k_1 h_e$ is small, the distance between two adjacent dashed lines is very small compared to the serration wavelength. Thus, even though pronounced phase differences appear along the edge, one can hardly see any phase variations within a spanwise correlation length. The pressure distribution for $k_1 h_e = 2$ is shown in figure 13(b) and no significant phase variations are achieved. However, for $k_1 h_e = 4$ a clear phase variation of
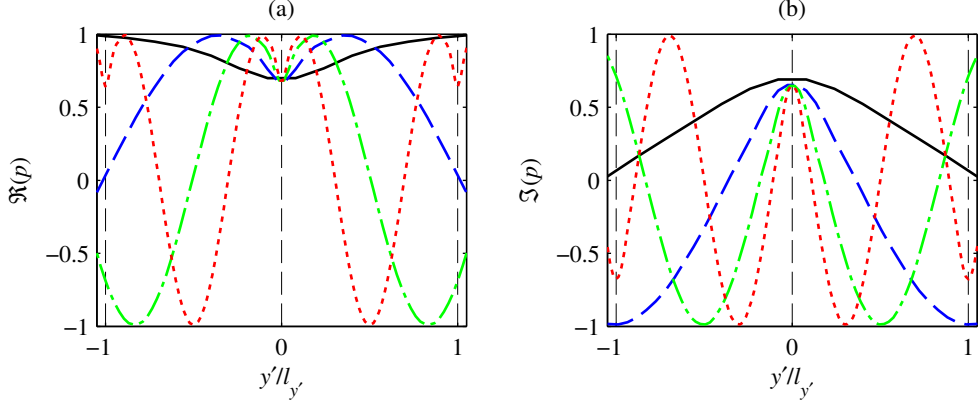
FIGURE 14. Scattered pressure on the serrated edge for different serration geometries with black solid line for $k_1h_3 = 1$, blue dashed line for $k_1h_e = 3$, green dot-dashed line for $k_1h_e = 6$ and red dotted line for $k_1h_e = 10$. (a): real part; (b): imaginary part.

scattered pressure begins to appear within adjacent lines, as shown in figure 13(c). From figure 13(d), where $k_1h_3 = 10$, it can be seen that pronounced phase differences appear within a correlation length $l_{y'}$ in the spanwise direction. To better visualize the phase variation appearing in the spanwise direction due to serrations, the scattered pressure along the serrated edge is shown in figure 14 for the same values of k_1h_e as in figure 13. Both the real and imaginary parts of the scattered pressure are presented. The tendency for large values of k_1h_e to favor strong phase variations is clearly demonstrated.

Finally, one is in a position to discuss the noise reduction mechanism by investigating the physical implications of the two parameters k_1h and k_1h_e. From figure 11 it is obvious that the criterion $k_1h \gg 1$ ensures an effective phase variation appearing along and near the trailing-edge in the spanwise direction. In addition, as shown from figure 13, the condition $k_1h_e \gg 1$ ensures that the phase difference appears within one spanwise correlation length, i.e. between two adjacent dashed lines shown in figure 11 and 13. Since the surface pressure within the regions bordered by dashed lines is coherent, and since the range over which the phase difference appears is clearly much smaller than the acoustic wavelength, the far-field sound will be reduced due to destructive interference. Physically, this means that the phase differences induced on the flat plate in the spanwise direction due to the presence of serrations should be well situated within a correlated turbulent structure. Therefore, as demonstrated in both figures 11 and 13, the sound reduction is caused by the destructive interference of the scattered surface pressure due to the presence of serrations.

Results in Sec. 3.2 have shown that in the case of wide serrations, a noise increase at low frequencies is also possible, especially at high Mach numbers. The reason is that at low frequencies, only little phase variation is induced by the presence of serrated trailing-edges in the spanwise direction, but the wetted length of the trailing-edge is in fact much longer than that of a straight one. Thus, the net effect of phase interference can be constructive, which leads to an increase in the far-field noise. This is more likely to occur when k_1h is small, i.e. M_0 is large, frequency is low or the serration is wide (small value of h).

Based on the preceding discussions, one can conclude that the minimum effective serration length required for noise reduction can be obtained from $h_{min} = \min(h, h_e)$. It is then straightforward to combine the two conditions stated above into one, i.e. $k_1h_{min} \gg$

1. Therefore, in order to achieve an effective noise reduction in the far-filed, the geometry of the serrations should satisfy $k_1 h_{min} \gg 1$. Based on the interference results in figure 11 and 13, it can be found that a common rule of thumb is $k_1 h_{min} \gtrsim \pi$, with higher value more favourable.

6. Conclusion

A new mathematical model is developed in this paper to predict the sound radiated by serrated trailing-edges. The model begins with establishing an idealized scattering problem, resulting in a mixed boundary value convective wave equation problem with complex boundaries. This leads to a set of coupled partial differential equations, which cannot be solved using the standard separation method. A solution is obtained based on Fourier expansion to separate the variables and Schwarzschild's method together with an iterative technique to solve the resulting coupled equations. The far-field sound is evaluated using the surface pressure integrals. The PSD of far-field sound is related to the wavenumber spectral density of the wall pressure beneath the turbulent boundary layer near the trailing-edge using Amiet's approach (Amiet 1976*b*, 1978).

The results obtained using the new model agree well with FEM computations, suggesting that the model developed in this paper captures the scattering process and gives correct predictions for the sound generated by serrated trailing-edges. It is shown that the coupling effect must not be ignored and as a result the new model can predict the sound reduction more accurately than Howe's model (Howe 1991*b,a*). The results obtained using the new model agree better with experiments, in which the average sound reduction is reported to be up to around 7 dB. The directivity results show that serrations can significantly reduce the noise in the area near the leading edge and that at high Mach numbers the use of serrations can lead to noise increase at small angles.

The physical mechanism for noise reduction is found to be interference effects in the wall pressure fluctuations due to the presence of serrations. Two non-dimensional parameters are found to be critical. First, $k_1 h \gg 1$ to ensure the existence of strong phase variation in the spanwise direction. Second, $k_1 h_e \gg 1$ to ensure that the phase differences along the edges are correlated in the spanwise direction. The sound reduction generally increases as the serration sharpness increases, but if the serrations are already sharp enough, further increasing the slope only affects high frequencies.

The results obtained using Chase's turbulent boundary layer spectrum model do not appear to explain the noise increase observed in experiments at high frequencies (Parchen *et al.* 1999; Oerlemans *et al.* 2009; Gruber 2012). This suggests that the wavenumber-frequency spectra of the surface pressure fluctuations (see Sec. 2.4) are not accurate or that this noise increase is due to some other mechanisms, such as the high intensity flow through serration valleys. In addition, the current model assumes perfect correlations in the streamwise direction, which may not be sufficiently accurate according to the measurements of Gruber (2012). Thus, the current model may be further improved by incorporating more physical parameters such as the streamwise correlation length.

Appendix A.

A.1. *Scattered pressure of second iteration*

The solution after the second iteration can be expressed as,

$$\boldsymbol{P}^{(2)}(x,0) = \boldsymbol{N}(x) + \boldsymbol{C}^{(1)}(x) + \boldsymbol{C}^{(2)}(x), \tag{A 1}$$

where $\boldsymbol{N}(x)$ and $\boldsymbol{C}^{(1)}(x)$ are defined in Sec. 2, and $\boldsymbol{C}^{(2)}(x)$ whose entry corresponding to mode n' is

$$
\begin{aligned}
C_{n'}^{(2)}(x) = {} & P_i(1-i)\mathrm{e}^{ik_1 x} \sum_{m=-\infty}^{\infty} \left\{ \beta_{n'm}(ik_1)^2 (\mathrm{E}(-\mu_{n'}x) - \mathrm{E}(-\mu_m x)) \right. \\
& - \left(\beta_{n'm}ik_1 + \gamma_{n'm}i(k_1-\mu_m)\right)\sqrt{\frac{\mu_m}{-2\pi x}}(\mathrm{e}^{-i\mu_{n'}x} - \mathrm{e}^{-i\mu_m x}) \\
& \left. - \frac{\gamma_{n'm}}{2}\left(\sqrt{\frac{\mu_m}{-2\pi x}}\frac{1}{(-x)}(\mathrm{e}^{-i\mu_{n'}x} - \mathrm{e}^{-i\mu_m x}) - i(\mu_{n'}-\mu_m)\sqrt{\frac{\mu_m}{-2\pi x}}\mathrm{e}^{-i\mu_{n'}x}\right) \right\},
\end{aligned}
\tag{A 2}
$$

where

$$\beta_{ln} = \sum_{m=-\infty}^{\infty} \left(v_{ln}a_m - B_{lm}a_n/(k_{2l}^2 - k_{2n}^2)\right)v_{nm},$$

$$\gamma_{ln} = \sum_{m=-\infty}^{\infty} \left(v_{ln}a_m\sqrt{\mu_m/\mu_n} - B_{lm}a_n/(k_{2l}^2 - k_{2n}^2)\right)v_{nm}.$$

A.2. *Far-field sound pressure of second iteration*

The function T_{nm} involved in the second iteration can be defined as:

$$
\begin{aligned}
T_{nm} = {} & \sum_{j=0}^{1} \frac{1}{i\kappa_{nj}} \left\{ \left(\frac{i\eta_{Am}}{\sqrt{\eta_{Am}}}\left(\mathrm{e}^{i\kappa_{nj}\chi_{j+1}}\mathrm{E}(\eta_{Am}(c+\epsilon_{j+1})) - \mathrm{e}^{i\kappa_{nj}\chi_j}\mathrm{E}(\eta_{Am}(c+\epsilon_j))\right) \right.\right. \\
& - \frac{i\eta_{Bmj}}{\sqrt{\eta_{Bmj}}}\mathrm{e}^{i\kappa_{nj}(\chi_j-(c+\epsilon_j)/\sigma_j)}\left(\mathrm{E}(\eta_{Bmj}(c+\epsilon_{j+1})) - \mathrm{E}(\eta_{Bmj}(c+\epsilon_j))\right)\right) - \\
& \left(\left(\mathrm{e}^{i\kappa_{nj}\chi_{j+1}}\frac{1}{\sqrt{2\pi(c+\epsilon_{j+1})}}\mathrm{e}^{i\eta_{Am}(c+\epsilon_{j+1})} - \mathrm{e}^{i\kappa_{nj}\chi_j}\frac{1}{\sqrt{2\pi(c+\epsilon_j)}}\mathrm{e}^{i\eta_{Am}(c+\epsilon_j)}\right)\right. \\
& \left.\left.- \mathrm{e}^{i\kappa_{nj}(\chi_j-(c+\epsilon_j)/\sigma_j)}\left(\frac{1}{\sqrt{2\pi(c+\epsilon_{j+1})}}\mathrm{e}^{i\eta_{Bmj}(c+\epsilon_{j+1})} - \frac{1}{\sqrt{2\pi(c+\epsilon_j)}}\mathrm{e}^{i\eta_{Bmj}(c+\epsilon_j)}\right)\right)\right\},
\end{aligned}
\tag{A 3}
$$

The second iterated solution falls into the same pattern,

$$
\begin{aligned}
p^{(2)}(\mathbf{x},\omega) = {} & \frac{-i\omega x_3}{4\pi c_0 S_0^2}P_i\mathrm{e}^{-ik(Mx_1-S_0)/\beta^2}\mathrm{e}^{ik(M-x_1/S_0)h/\beta^2}(1-i)\times \\
& \frac{\sin\left((N+1/2)\lambda(k_2 - kx_2/S_0)\right)}{\sin\left((k_2 - kx_2/S_0)\lambda/2\right)} \sum_{n'=-\infty}^{\infty}\left(\Theta_{n'} + \Theta_{n'}^{(1)} + \Theta_{n'}^{(2)}\right),
\end{aligned}
\tag{A 4}
$$

where $\Theta_{n'}$ and $\Theta_{n'}^{(1)}$ are defined in Sec. 2, and

$$\Theta_{n'}^{(2)} = \sum_{m=-\infty}^{\infty} \beta_{n'm}(ik_1)^2(Q_{n'n'} - Q_{n'm}) - (\beta_{n'm}\sqrt{\mu_m}ik_1 + \gamma_{n'm}\sqrt{\mu_m}i(k_1 - \mu_m))(S_{n'n'} - S_{n'm})$$
$$- \gamma_{n'm}\sqrt{\mu_m}\big(T_{n'n'} - T_{n'm} - i(\mu_{n'} - \mu_m)S_{n'n'}/2\big). \tag{A5}$$

REFERENCES

AMIET, R. K. 1975 Acoustic radiation from an airfoil in a turbulent stream. *Journal of Sound and Vibration* **41** (4), 407–420.

AMIET, R. K. 1976*a* High frequency thin-airfoil theory for subsonic flow. *AIAA Journal* **14** (8), 1076–1082.

AMIET, R. K. 1976*b* Noise due to turbulent flow past a trailing edge. *Journal of Sound and Vibration* **47** (3), 387–393.

AMIET, R. K. 1978 Effect of the incident surface pressure field on noise due to turbulent flow past a trailing edge. *Journal of Sound and Vibration* **57**, 305–306.

AZARPEYVAND, M., GRUBER, M. & JOSEPH, P. F. 2013 An analytical investigation of trailing edge noise reduction using novel serrations. In *Proceedings of 19th AIAA/CEAS Aeroacoustics Conference*. Berlin, Germany.

CALLENDER, B., GUTMARK, E. J. & MARTENS, S. 2005 Far-field acoustic investigation into chevron nozzle mechanisms and trends. *AIAA Journal* **43** (1), 87–95.

CASALINO, D., DIOZZI, F., SANNINO, R. & PAONESSA, A. 2008 Aircraft noise reduction technologies: a bibliographic review. *Aerospace Science and Technology* **12**, 1–17.

CHASE, D. M. 1975 Noise radiated from an edge in turbulent flow. *AIAA journal* **13**, 1041–1047.

CHASE, D. M. 1987 The character of the turbulent wall pressure spectrum at subconvective wavenumbers and a suggested comprehensive model. *Journal of Sound and Vibration* **112**, 125–147.

CORCOS, G. M. 1964 The structure of the turbulent pressure field in boundary-layer flows. *Journal of Fluid Mechanics* **18**, 353–378.

CURLE, N. 1955 The influence of solid boundaries upon aerodynamic sound. *Proceedings of the Royal Society A: Mathematical, Physical and Engineering Sciences* **231**, 505–514.

DASSEN, A. G. M., PARCHEN, R., BRUGGEMAN, J. & HAGG, F. 1996 Results of a wind tunnel study on the reduction of airfoil self-noise by the application of serrated blade trailing edges. *Proceeding of the European Union Wind Energy Conference and Exhibition* pp. 800–803.

ECKERT, E. R. & DRAKE, R. M. 1959 *Heat and mass transfer*. New York: McGraw-Hill.

GRUBER, M. 2012 Airfoil noise reduction by edge treatments. PhD thesis, University of Southampton, Southampton, UK.

GRUBER, M., JOSEPH, P. F. & AZARPEYVAND, M. 2013 An experimental investigation of novel trailing edge geometries on airfoil trailing edge noise reduction. In *Proceedings of 19th AIAA/CEAS Aeroacoustics Conference*. Berlin, Germany.

HOWE, M. S. 1991*a* Aerodynamic noise of a serrated trailing edge. *Journal of Fluids and Structures* **5**, 33–45.

HOWE, M. S. 1991*b* Noise produced by a sawtooth trailing edge. *The Journal of the Acoustical Society of America* **90**, 482–487.

JONES, L. E. & SANDBERG, R. D. 2012 Acoustic and hydrodynamic analysis of the flow around an aerofoil with trailing-edge serrations. *Journal of Fluid Mechanics* **706**, 295–322.

LAMB, H. 1932 *Hydrodynamics*, 6th edn. New York: Dover Publications.

LIGHTHILL, M. J. 1952 On sound generated aerodynamically. I. General theory. *Proceedings of the Royal Society A: Mathematical, Physical and Engineering Sciences* **211**, 564–587.

MOREAU, D. J. & DOOLAN, C. J. 2013 Noise-reduction mechanism of a flat-plate serrated trailing edge. *AIAA journal* **51**, 2513–2522.

OERLEMANS, S., FISHER, M., MAEDER, T. & KÖGLER, K. 2009 Reduction of wind turbine noise using optimized airfoils and trailing-edge serrations. *AIAA journal* **47**, 1470–1481.

OERLEMANS, S., SIJTSMA, P. & MÉNDEZ LÓPEZ, B. 2007 Location and quantification of noise sources on a wind turbine. *Journal of Sound and Vibration* **299** (4C5), 869 – 883.

PARCHEN, R., HOFFMANS, W., GORDNER, A. & BRAUN, K. 1999 Reduction of airfoil self-noise at low mach number with a serrated trailing edge. *International Congress on Sound and Vibration, 6th Technical Univ. of Denmark, Lyngby, Denmark* pp. 3433–3440.

ROGER, M. & CARAZO, A. 2010 Blade-geometry considerations in analytical gust-airfoil interaction noise models. In *Proceedings of 16th AIAA/CEAS Aeroacoustic Conference*. Stockholm, Sweden.

ROGER, M. & MOREAU, S. 2005 Back-scattering correction and further extensions of Amiet's trailing-edge noise model. Part 1: theory. *Journal of Sound and Vibration* **286**, 477–506.

ROGER, M., SCHRAM, C. & SANTANA, L. D. 2013 Reduction of airfoil turbulence-impingement noise by means of leading-edge serrations and/or porous materials. In *Proceedings of 19th AIAA/ CEAS Aeroacoustics Conference*, pp. 1–20. Berlin, Germany.

SÜLI, E. & MAYERS, D. 2003 *An introduction to numerical analysis*. Cambridge, UK: Cambridge University Press.

WILLIAMS, J. E. & HALL, L. H. 1970 Aerodynamic sound generation by turbulent flow in the vicinity of a scattering half plane. *Journal of Fluid Mechanics* **40**, 657–670.

WILLMARTH, W. W. 1959 Space-time correlations and spectra of wall pressure in a turbulent boundary layer. *NASA Tech Memo 3-17-59W* .

YAN, J., PANEK, L. & THIELE, F. 2007 Simulation of jet noise from a long-cowl nozzle with serrations. In *Proceedings of 13th AIAA/CEAS Aeroacoustics Conference*. Rome, Italy.